Multiple sulfur isotope signals associated with the late Smithian event and the Smithian/Spathian boundary.

Christophe Thomazo, Arnaud Brayard, S. Elmeknassi, Emmanuelle Vennin, Nicolas Olivier, Gwénaël Caravaca, Gilles Escarguel, Emmanuel Fara, Kevin G. Bylund, James F. Jenks, et al.

HAL Id: hal-02270774

https://hal.science/hal-02270774

Submitted on 20 Dec 2021

1   **Multiple sulfur isotope signals associated with the late Smithian event and**

2   **the Smithian/Spathian boundary**

3

4   C. Thomazo[1,*], A. Brayard[1], S. Elmeknassi[1], E. Vennin[1], N. olivier[2], G. Caravaca[1], G.

5   Escarguel[3], E. Fara[1], K.G. Bylund[4], J.F. Jenks[5], D.A. Stephen[6], B. Killingsworth[7], P.

6   Sansjofre[7], P. Cartigny[8]

7

8   [1]Laboratoire Biogéosciences, UMR 6282, CNRS, Université Bourgogne Franche-Comté,

9   21000 Dijon, France

10   [2]Université Clermont Auvergne, CNRS, Laboratoire Magmas et Volcans, F-63000 Clermont-

11   Ferrand, France

12   [3]Laboratoire d'Ecologie des Hydrosystèmes Naturels et Anthropisés, UMR 5023, CNRS,

13   Université de Lyon, 69622 Villeurbanne Cedex, France.

14   [4]140 South 700 East, Spanish Fork, Utah 84660, USA

15   [5]1134 Johnson Ridge Lane, West Jordan, Utah 84084, USA

16   [6]Department of Earth Science, Utah Valley Univ., Orem, Utah 84058, USA

17   [7]CNRS-UMR6538 Lab. Géosciences Océan, Université de Bretagne Occidentale, 29280

18   Plouzané, France

19   [8]Institut de Physique du Globe de Paris, Sorbonne-Paris Cité, Univ. Paris Diderot, CNRS,

20   75238 Paris Cedex 05, France

21

22   *Corresponding author: christophe.thomazo@u-bourgogne.fr

23

24

25

26   **Abstract**

27   The Early Triassic is generally portrayed as a time of various, high ecological stresses

28   leading to a delayed biotic recovery after the devastating end-Permian mass extinction. This

29   interval is notably characterized by repeated biotic crises (e.g., during the late Smithian),

30   large-scale fluctuations of the global carbon, nitrogen and sulfur cycles as well as harsh

31   marine conditions including a combination of ocean acidification, anoxia, extreme seawater

32   temperatures and shifting productivity. Observations from different paleolatitudes suggest

33   that sulfidic (H_2S-rich) conditions may have developed widely during the Early Triassic,

34   possibly reaching up to ultra-shallow environments in some places. However, the existence

35   and the spatio-temporal extent of such redox swings remain poorly constrained. In order to

36   explore Early Triassic paleoceanographic redox changes and their potential influences on the

37   biotic recovery, we analyzed multiple sulfur isotopes (^{32}S, ^{33}S, ^{34}S, and ^{36}S) of sedimentary

38   pyrite and carbonate associated sulfate ($\delta^{34}S_{CAS}$) from the Mineral Mountains section, Utah.

39   Sediments from this section were mainly deposited in shallow waters and span the Smithian

40   and lower Spathian. We report a 68‰ range of variations in $\delta^{34}S_{py}$ associated with $\Delta^{33}S_{py}$

41   varying from -0.01‰ to +0.12‰, whereas the $\delta^{34}S_{CAS}$ varies between +19.5‰ and +34.8‰.

42   We interpret the observed signal of multiple sulfur isotopes as reflecting the operation of

43   pore-water synsedimentary microbial sulfate reduction in open system with respect to sulfates

44   before the late Smithian, evolving to a closed system, sulfate limited, Rayleigh-type

45   distillation across the Smithian/Spathian boundary (SSB) and immediately after the SSB. We

46   argue that this marked change is driven by the effectiveness of the connection between the

47   sedimentary pore waters and the overlying water column, which is, in our case, controlled by

48   the local sedimentological conditions such as the bioturbation intensity and the sedimentation

49   rate. Therefore, our results suggest that changes in the sulfur cycle before and across the SSB

50   at Mineral Mountains is probably a local consequence of the loss of the mixed sedimentary

51   layer during the late Smithian extinction event, as opposed to reflecting the development of a

52   lethal anoxic ocean at the global scale.

53

54   **1. Introduction**

55   *1.1. Smithian and Smithian/Spathian boundary events*

56   The recovery of marine and terrestrial ecosystems after the end-Permian mass

57   extinction (EPME, ~252 Ma) is usually described as a slow and delayed process resulting

58   from the effects of sustained or recurrent environmental stresses during the Early Triassic,

59   such as extreme climatic warmings (Sun et al., 2012; Romano et al., 2013), intensified water-

60   column stratifications (Horacek et al., 2007; Song et al., 2013) and expansions of oceanic

61   oxygen-minimum zones (Algeo et al., 2010, 2011; Winguth and Winguth, 2012). Although

62   oxygen deficiency was probably a major biotic stressor in the thermocline and deep-ocean,

63   shallow-marine environments were generally well-oxygenated except for brief anoxic

64   episodes (Algeo et al., 2007, 2008; Beatty et al., 2008; Zonneveld et al., 2010). Specifically,

65   extremely harsh environmental conditions were suggested during the late Smithian (~1.4 Ma

66   after the Permian/Triassic boundary, PTB; Galfetti et al., 2007a) as this short time interval

67   (~100 kyr, Brühwiler et al., 2010) records a severe extinction of the nekton (e.g., Orchard,

68   2007, Brayard et al., 2006, 2009; Stanley, 2009). Major disturbances in the global carbon

69   cycle in the Smithian and through the Smithian/Spathian boundary (SSB) are documented by

70   a strong negative-positive couplet of carbon isotope excursions respectively before and during

71   the late Smithian. This couplet of excursions is documented worldwide in both carbonate

72   ($\delta^{13}C_{carb}$) and organic ($\delta^{13}C_{org}$) carbon reservoirs (Payne et al., 2004; Galfetti et al., 2007a and

73   b; Tong et al., 2007; Horacek et al., 2009; Hermann et al., 2011; Clarkson et al., 2013;

74   Komatsu et al., 2016; Fig. 1). However, the magnitude differs from section to section and

75   depends on the reservoir that has been measured (e.g., Meyer et al., 2011; Grasby et al., 2013;

3

76   Song et al., 2013; Thomazo et al., 2016; Caravaca et al., 2017a). The negative shift is usually

77   attributed to a massive light carbon input and/or a major reorganization of the exogenous

78   global carbon cycle, such as a decrease in the organic carbon flux buried in the sedimentary

79   record. The negative shift has thus been linked to an episodic large-scale injection into the

80   atmosphere of volcanic CO_2 and thermogenic CH_4 from the Siberian Traps (Payne et al.,

81   2004; Payne and Kump, 2007; Meyer et al., 2011; Sobolev et al., 2011). Alternatively, local

82   processes such as early diagenetic reactions in pore water producing authigenic carbonates

83   also probably participate to generate this signal (Thomazo et al., 2016; Zhao et al., 2016). The

84   negative isotopic excursion is followed by an abrupt positive $\delta^{13}C$ excursion of comparable

85   magnitude beginning in the late Smithian and crossing the SSB. Such negative-positive

86   swings in the carbon isotope record were suggested to characterize strong anoxic conditions

87   (e.g., Retallack and Jahren, 2008; Song et al., 2012; 2014a). Positive covariation of this

88   oscillation in the $\delta^{13}C_{carb}$ signal with existing $\delta^{34}S_{CAS}$ records has been interpreted to reflect

89   changes in the burial rate of sedimentary sulfides during increased marine anoxia in an ocean

90   with an extremely small sulfate reservoir (Song et al., 2010; 2014b). Late Smithian potential

91   anoxic sediments were reported from various localities worldwide (e.g., Galfetti et al., 2008;

92   Grasby et al., 2013) and anoxic conditions possibly reached ultra-shallow environments in

93   some places (e.g., Wignall et al., 2016).

94   The late Smithian and the SSB are also marked by a major shift in climate, changing

95   from hot to cool conditions (Sun et al., 2012; Romano et al., 2013). This event corresponds to

96   major changes in marine and terrestrial organisms (Tozer, 1982; Dagys, 1988; Galfetti et al.,

97   2007a and b; Hermann et al., 2011; Schneebli-Hermann et al., 2012), including for instance a

98   severe drop in taxonomic richness and disparity among ammonoids (Stanley, 2009; Brayard

99   et al., 2009; Brosse et al., 2013), and a major restructuring of their biogeographical

100   distributions (e.g. Brayard et al., 2006, 2007; Jattiot et al., 2016). The late Smithian extinction

101   was at least of equal magnitude to the EPME for ammonoids (e.g., Brühwiler et al., 2010;

102   Jattiot et al., 2016). However, recent works showed that in some shallow-water settings of the

103   Panthalassa, environmental conditions were favorable to the development of diversified and

104   complex ecosystems during the earliest Spathian, i.e., immediately after the SSB (Brayard et

105   al., 2017).

106

107   *1.2. Potential underlying processes*

108   Carbon isotopic trends during the Smithian-Spathian transition have been interpreted

109   in various ways. A first scenario suggests that emissions of ^{12}C-enriched carbon dioxide

110   associated with the Siberian Traps (Payne et al., 2004; Payne and Kump, 2007), causing an

111   acidification, a warming trend and an oceanic anoxia (Galfetti et al., 2008; Grasby et al.,

112   2013; Song et al., 2014a; Clarkson et al., 2016). The subsequent enhanced burial of

113   isotopically light organic carbon in anoxic sediments would have generated the positive δ^{13}C

114   trend documented across the SSB (Galfetti et al., 2007a). In a second model, Meyer et al.

115   (2011) argued that the positive δ^{13}C shift records an increased productivity in the water

116   column thereby generating a steeper surface-to-deep isotopic gradient. In a third alternative,

117   Horacek et al. (2007) interpreted the initial negative shift as reflecting the overturn of a

118   previously well-stratified ocean water column causing the release of light dissolved inorganic

119   carbon, derived from remineralized organic matter (OM) into the upper water column. Finally,

120   local early diagenetic reactions in pore water producing ^{12}C-enriched authigenic carbonates

121   during the suboxic remineralization of OM due to microbial sulfate reduction have also been

122   suggested (Thomazo et al., 2016; Zhao et al., 2016). All these hypotheses differ in their

123   predictions on the relative timing of the carbon isotope excursions and anoxia. The scenario

124   of Galfetti et al.'s (2007a) implies that anoxia developed concomitantly to the positive shift

125   during the late Smithian; the Meyer et al.'s (2011) scenario corresponds to an anoxia peaking

126   later when $\delta^{13}C$ reaches maximum values; the Horacek et al.'s (2007) model suggests that

127   anoxia peaked just prior to the minimum in $\delta^{13}C$. Finally, the diagenetic hypothesis supports

128   the synsedimentary co-occurrence of suboxic conditions and of the minimum $\delta^{13}C$ values,

129   which do not involve a water-column process. Therefore, the relationships between redox

130   changes, $\delta^{13}C$ fluctuations, and biotic events around the SSB needs further investigations and

131   better discrimination between synsedimentary *versus* water-column chemical processes.

132

133   *1.3. The biogeochemical sulfur cycle, oceanic redox conditions and sulfur isotopes*

134   The biogeochemical sulfur cycle is a key process in regulating Earth's surface

135   environment through the activity of several microbial metabolisms including primarily sulfate

136   reduction, disproportionation, and sulfide oxidation. These metabolic activities transform the

137   oxidation state of sulfur and are tightly linked to the global carbon cycle and climate, through

138   the remineralization of organic carbon in marine sediments. The burial of oxidized (sulfate)

139   relative to reduced (sulfide) minerals on the geological time scale, in marine sediments and

140   sedimentary rocks, regulates marine redox conditions (Berner and Raiswell, 1983; Canfield,

141   2001). The various microbial pathways that drive the sulfur cycle can be recognized using

142   their diagnostic stable isotopic fractionations of sulfur species (Chambers et al., 1975; Fry et

143   al., 1984; Canfield and Thamdrup, 1994; Habicht and Canfield, 1997; Habicht et al., 1998;

144   Brunner and Bernasconi, 2005; Johnston et al., 2005a; Sim et al., 2011a, b). In modern

145   environments, the isotopic compositions of aqueous sulfide and sulfate have been

146   successfully used to demonstrate specific biological sulfur cycling activities (e.g. Canfield et

147   al., 2010; Fike et al., 2008, 2009; Gomes and Hurtgen, 2013). In ancient sediments, the

148   isotopic record of sulfur-bearing phases, predominantly sulfate minerals in the form of barite

149   and CAS as well as sulfides in the form of pyrite, can be also used to trace sulfur metabolisms

150   (Canfield and Teske, 1996; Shen et al., 2001; Johnston et al., 2005b; Philippot et al., 2007;

151 Leavitt et al., 2013) and to reconstruct the past ocean chemistry and oxidation state (Claypool

152 et al., 1980; Canfield and Teske, 1996; Johnston et al., 2005b; Fike et al., 2006; Gill et al.,

153 2007; Fike and Grotzinger, 2008; Hurtgen et al., 2009; Jones and Fike, 2013).

154   The two main components driving the long-term secular fluctuation of δ^{34}S of sulfur

155 species over geological time are variations in the net flux of sulfate reduced to sulfide,

156 subsequently precipitated as pyrite in marine sediments, and the mean isotopic fractionation

157 between marine sulfate and sedimentary pyrite produced during the microbial metabolic

158 activities (Fike et al., 2015). For example, during times of increased pyrite burial enhanced by

159 protracted marine anoxia, the δ^{34}S of marine sulfates would increase generating a positive

160 isotopic excursion imprint in both sulfate and sulfide reservoirs. Modulation of sedimentary

161 sulfides burial can also influence the size of the oceanic dissolved sulfate reservoir, and hence,

162 the kinetic of sulfur isotope variations (Bottrell and Newton, 2006). When the oceanic sulfate

163 reservoir is small, rapid δ^{34}S variations can thus be driven by relatively small flux imbalances.

164   Meanwhile, depositional environment and sediment remobilization can have

165 considerable impacts on the isotopic composition of both pore water and sedimentary sulfate

166 and sulfide phases (Aller et al., 2008, 2010). Bioturbation and the local sedimentation rate can

167 also impact the sulfur isotope records by decoupling the evolution of sedimentary pyrite δ^{34}S

168 to the overlying water column (Pasquier et al., 2017). Moreover, both sulfate and pyrite sulfur

169 isotope signals can be muted during diagenesis. Record of the $\delta^{34}S_{CAS}$ can notably be altered

170 by circulating fluids (e.g., meteoric fluids) during diagenetic secondary carbonate

171 precipitation and can obscure the signal of the primary oceanic sulfate isotopic composition.

172 Additionally, post-depositional processes can impact the $\delta^{34}S_{py}$ records. For instance, $\delta^{34}S_{py}$

173 signatures can be overprinted during late-stage diagenesis when sulfide-bearing fluids migrate

174 through strata that contain reactive iron (Fike et al., 2015). Due to these various possible

175 secondary imprints on the sedimentary sulfur isotope signals, a full characterization of the

176   depositional environment in which the sample formed is mandatory, as well as an evaluation

177   of its connection to the open ocean, and of its diagenetic history (Fike et al., 2015).

178   In addition to the $\delta^{34}S$ record of sulfur species, the measurement of multiple sulfur

179   isotopes (MSI) recently becomes increasingly important to further constrain the Phanerozoic

180   evolution of the biogeochemical sulfur cycle (Wu et al., 2010), as well as in modern

181   environments (e.g., Tostevin et al., 2014). The use of pyrite $\delta^{33}S$ in addition to $\delta^{34}S$ can

182   provide additional ways to evaluate the involvement of different sulfur metabolisms, as well

183   as variations in sulfur fluxes through geologic time (Johnston et al., 2005a, 2005b, 2007,

184   2008a, b; Ono et al., 2006; Li et al., 2010; Wu et al., 2010; Zerkle et al., 2010; Shen et al.,

185   2011; Leavitt et al., 2013; Sansjofre et al., 2016). Furthermore, MSI is a robust tool to

186   investigate Phanerozoic paleoredox conditions even when the pyrite and contemporaneous

187   seawater sulfate $\delta^{34}S$ measurements are not paired in the same samples (Shen et al., 2011;

188   Zhang et al., 2015, 2017; Saitoh et al., 2017). For paleoenvironmental reconstructions,

189   measurements of minor sulfur isotopes (^{33}S and ^{36}S) can provide additional information on

190   local and global processes and can be helpful for differentiating between these two cases

191   (Johnston et al., 2006; Saitoh et al., 2017).

192   Therefore, the MSI composition of seawater sulfates and precipitated sulfides (i.e.,

193   pyrite) can be an important proxy to discuss the Smithian-Spathian transition processes.

194   Previous studies focusing on this time interval and aiming to reconstruct the biogeochemical

195   sulfur cycle were based on analyses of pyrite framboids and trace metal elements from South

196   China (Tian et al., 2014; Sun et al., 2015), iron mineral speciation from the Arabian margin

197   (Clarkson et al., 2016), carbonate associated sulfate (CAS) $\delta^{34}S$ signal from South China

198   (Zhang et al., 2015) and the western USA (Marenco et al., 2008), sulfide $\delta^{34}S$ signal from

199   Japan (Takahashi et al., 2013), barite and evaporite $\delta^{34}S$ signal from Italy (Cortecci et al.,

200   1981; Horacek et al., 2010), and paired sulfur isotopes (CAS and pyrite) signals from South

8

201   Central China (Song et al., 2014b). Although the CAS δ^{34}S values in recent sediments are in

202   agreement with the sulfur isotopic composition of modern seawater sulfates (Lyons et al.,

203   2004), and while the record of ancient carbonates is more complete than the record of marine

204   evaporites, the fidelity of CAS signals in rocks that have undergone variable degrees of

205   secondary processes (e.g., early or burial diagenesis, hydrothermal alteration) needs to be

206   carefully testified for each measured section and sample (Present et al., 2015). For instance,

207   Marenco et al. (2008) performed δ^{34}S$_{CAS}$ measurements on samples from the Early Triassic

208   Moenkopi Formation of the Sonoma Foreland (western USA) basin and showed that an

209   alteration of the isotopic signal during late stage dolomitization could not be fully excluded.

210   In this study, we test the existence of anoxia during the late Smithian and its

211   relationships with the Smithian-Spathian δ^{13}C curve by measuring the MSI of sedimentary

212   sulfides and ^{34}S/^{32}S sulfur isotopes of CAS in the shallow water deposits of the Mineral

213   Mountains section, Utah, USA. This section has been previously studied for its sedimentary

214   and fossil contents, as well as for its paired carbon isotope signal (Brayard et al., 2011, 2015;

215   Hofmann et al., 2014; Vennin et al., 2015; Thomazo et al., 2016). We discuss results of our

216   sulfur isotope analyses in the light of detailed sedimentological constraints on depositional

217   environments, within global C cycle perturbations typical of the late Smithian and SSB, to

218   provide new insights into the nature of oceanic and sedimentary environmental changes at

219   that time.

220

221   **2. Geological setting**

222   *2.1. The Sonoma Foreland Basin*

223   During the Permian-Triassic transition, the Sonoma orogeny led to the formation of

224   the Sonoma Foreland Basin (SFB) (Fig. 2; Burchfiel and Davis, 1975; Ingersoll, 2008;

225   Dickinson, 2013; Caravaca et al., 2017b). This sedimentary basin extends from the modern

226   states of Idaho and Wyoming to Utah and eastern Nevada. The SFB was located in the

227   northern intertropical zone on the western Pangea margin during the Early Triassic (Fig. 2).

228   The SFB shows detailed and well-preserved Lower Triassic fossil and sedimentary records

229   with mainly transitional continental/marine terrigenous conglomerates and sandstones of the

230   Moenkopi Group to shallow marine carbonates of the Thaynes Group (e.g., Kummel, 1954,

231   1957, Paull and Paull, 1993; Lucas et al., 2007). A robust, high-resolution, Smithian

232   biostratigraphic framework based on ammonoids is available for most parts of the basin

233   (Brayard et al., 2009, 2013; Jattiot et al., 2016, 2017; Jenks and Brayard, 2018).

234

235   *2.2. The Mineral Mountains section*

236   The alternating carbonates and marls of the Lower Triassic Thaynes Group (*sensu*

237   Lucas et al., 2007) reflect sedimentary deposition in epicontinental marine environments and

238   rest unconformably on middle to upper Permian rocks with a major sedimentary hiatus

239   corresponding to the Permian-Triassic transition (e.g., McKee, 1954; Collinson et al., 1976).

240   In western and central Utah, the late Permian, Griesbachian and Dienerian are usually not

241   observed. The historical middle and late Smithian time markers of the Thaynes Group within

242   the SFB are respectively the *Meekoceras* and *Anasibirites* ammonoid zones, but these zones

243   can be further subdivided (see discussion in Brayard et al., 2009, 2013; Jattiot et al. 2016;

244   Jenks and Brayard, 2018).

245   The present study has been carried out on the Smithian to Spathian sedimentary

246   succession in the Mineral Mountains, thoroughly described for its sedimentological

247   characteristics by Vennin et al. (2015; Figs. 2, 3). The basal unit A mostly consists of

248   microbially-dominated carbonates with sponge-microbe bioconstructions deposited on a

249   mudflat inner ramp, intertidal to supratidal, environments evolving upward into bioclastic

250   sediments deposited in tidal-dominated shoreface environments. Mudstone-rich sediments of

251 the unit B are finely laminated and reflect homogenous upper offshore depositional conditions

252 of outer to mid-ramp environments. They were episodically influenced by storm-induced

253 events (Fig. 3). The unit including the SSB ("unit SSB") is composed of marls representing

254 outer ramp, lower offshore, environments. This unit corresponds to the deepest deposits,

255 below the storm wave base. The overlying unit C evolves from mudstones deposited in outer

256 ramp (with local storm-induced deposits) to subtidal microbial carbonates deposited in outer

257 to mid ramp environments. The evolution prior to the SSB unit thus shows a progressive

258 deepening, whereas the lower Spathian corresponds to shallowing-upward conditions.

259 The local ammonoid biostratigraphy has been described in Brayard et al. (2011, 2013).

260 The unit A is early Smithian in age ("*Vercherites undulatus* beds"; *V.u.* in Fig. 3). The unit B

261 is latest early to middle Smithian in age (*Inyoites beaverensis* and *Owenites* beds,

262 respectively; *I.b.* and *O.* in Fig. 3; Unitary Association Zones UAZ_3 and UAZ_4 in Jattiot et al.,

263 2017). The SSB unit mainly corresponds to the late Smithian with the occurrence of typical

264 prionitid and xenoceltitid ammonoid assemblages (*A.m.* and *Xe*. in Fig. 3; UAZ_5 and UAZ_6 in

265 Jattiot et al., 2017). Although Spathian beds are not well identified above these late Smithian

266 assemblages, the first Spathian dominant fauna likely corresponds to a regional bivalve bloom

267 (Brayard et al., 2013; Hofmann et al., 2014).

268 The Early Triassic is marked by a global long-term rise in sea level with several

269 second- and third-order transgressive-regressive (T–R) sequences (Haq et al., 1987). Within

270 the SFB, a Spathian T-R cycle is recognized together with two older T-R cycles that

271 developed during the Griesbachian–Dienerian and the Smithian (e.g., Paull and Paull, 1993;

272 Lucas et al., 2007). The Smithian transgression proceeded southward in a complex pathway

273 resulting from the multifaceted subsidence of the basin and paleotopographic highs within

274 and on each side of the basin (e.g. Lucas et al., 2007; Caravaca et al., 2017b). The maximum

275 extent of this transgression within the basin was reached during the late Smithian (Paull and

276 Paull 1993; Lucas et al., 2007; Brayard et al., 2013). It corresponds to the deepest

277 environmental conditions recorded at Mineral Mountains, i.e., the unit SSB (Vennin et al.,

278 2015).

279

280 **3. Methods**

281 A total of 34 bulk rock samples of the Mineral Mountains section were investigated

282 for their major and trace elements, carbonate carbon isotopes, sulfide major (^{32}S, ^{33}S) and

283 minor (^{33}S, ^{36}S) sulfur isotopes and CAS major sulfur isotopes (Table 1). All measurements

284 were performed on bulk rock samples which were at start powdered to < 60 µm using a ring

285 and puck mill at the Biogéosciences Laboratory, Dijon, France.

286

287 *3.1. Carbonate carbon isotopes*

288 Carbonate carbon isotope analyses ($\delta^{13}C_{carb}$) were carried out at the Biogéosciences

289 Laboratory, Dijon, France. The samples (90 to 300 µg) were loaded into septum screwed

290 glass tubes, flushed via the autosampler with He to remove atmospheric gases. Each sample

291 was reacted with 500 µl of >100% phosphoric acid at 90°C for 17 min using an online

292 carbonate preparation line coupled to an IsoPrime stable isotope ratio mass spectrometer

293 (Isoprime, Manchester, UK). Inorganic carbonate content was quantified manometrically

294 from the CO_2 yield; all isotopic values are reported in the standard δ-notation in permil (‰)

295 relative to VPDB by assigning a $\delta^{13}C$ value of +1.95‰ to the NBS19 international standard.

296 The long-term reproducibility of the NBS19 replicate analyses (three months) is better than ±

297 0.09‰ (1σ) for carbon isotopes. H_3PO_4 blank tests were performed and evolved CO_2 was

298 below the detection limit of our online-IRMS system.

299

3.2. Sulfide isotopes

301   Sulfide sulfur was retrieved using a conventional wet chemical extraction at the

302   Biogéosciences Laboratory, Dijon, France. Acid volatile sulfide (AVS), representing

303   monosulfides, and chromium reducible sulfur (CRS) consisting primarily of pyrite were

304   extracted sequentially. First, AVS was liberated using cold concentrated HCl for 2 hours. If

305   any, resulting hydrogen sulfide was precipitated as Ag_2S with a 0.3 M $AgNO_3$ solution.

306   Subsequently, CRS was released using a hot and acidic 1.0 M $CrCl_2$ solution (Canfield et al.,

307   1986). The resulting H_2S was precipitated as Ag_2S. After centrifugation, the silver sulfide

308   precipitate was washed several times with deionized distilled water and dried at 50°C for 48

309   hours in an oven and weighted. Mass balance was used to calculate the amount of AVS and

310   CRS. Concentrations in ppm are reported individually in Table 1 (note that monosulfides

311   were below the detection limit in all samples). The silver sulfides were then fluorinated to

312   produce SF_6 and analyzed for their multiple sulfur isotope compositions at the Stable Isotope

313   Laboratory of the Institut de Physique du Globe de Paris, France. The isotope compositions

314   were determined by dual-inlet gas-source mass spectrometry monitoring ion beams at m/z of

315   127, 128, 129, and 131 using a ThermoScientific MAT 253 gas source mass spectrometer

316   (Labidi et al., 2012). Sulfur isotope ratios are reported in conventional delta notation with

317   respect to VCDT as Eq. (1):

318
$$\delta^{3i}S = \left(\frac{\left(\frac{^{3i}S}{^{32}S} \right)_{sample}}{\left(\frac{^{3i}S}{^{32}S} \right)_{V-CDT}} - 1 \right) \times 1000 \tag{1}$$

319   where *i* is either 3, 4 or 6;

320   and as Eqs. (2) and (3) for capital delta notation (following Johnston et al., 2008a):

321
$$\Delta^{33}S = \delta^{33}S - 1000 \cdot \left(\left(1 + \frac{\delta^{34}S}{1000} \right)^{0.515} - 1 \right) \tag{2}$$

$$\Delta^{36}S = \delta^{36}S - 1000 \cdot \left(\left(1 + \frac{\delta^{34}S}{1000} \right)^{1.90} - 1 \right) \qquad (3)$$

The δ^{34}S values are presented with an analytical reproducibility of ≤0.1‰. We used values for IAEA-S2 on the Vienna Cañon Diablo Troilite (VCDT) normalization of 5.224‰, 0.030‰ and −0.203‰ for δ^{34}S, Δ^{33}S, and Δ^{36}S, respectively. Based on duplicate and triplicate analyses, uncertainties on Δ^{33}S and Δ^{36}S values by the SF_6 technique are estimated at 0.01‰ and 0.2‰ in 2σ, respectively.

Ten samples have been successfully cross calibrated (Table 1, Fig. 4) for their $\delta^{34}S_{py}$ with measurements performed at the Biogéosciences Laboratory, Dijon, France, on SO_2 molecules via combustion of ~500 µg of silver sulfide homogeneously mixed with an equal amount of tungsten trioxide using a Vario PYRO cube (Elementar GmbH) connected online via an open split device to an IsoPrime IRMS system (Isoprime, Manchester, UK). International standards IAEA-S-1, IAEA-S-2 and IAEA-S-3 were used for calibration assuming δ^{34}S values of -0.3‰, +22.7‰ and -32.3‰ (VCDT), respectively. Analytical reproducibility was better than ± 0.3‰ (1σ) based on replicates for standard materials and samples.

3.3. CAS sulfur isotopes

CAS sulfur was retrieved using a wet chemical extraction at the Laboratory Géosciences Océan, Brest, France. Fifty grams of carbonate samples (with carbonate contents typically >70 wt. % of the total rock) were powdered, soluble sulfates being leached by a 1.7 M NaCl solution for 4 hours, followed by four rinses in deionized water. This step was repeated five times and the powder was then dissolved in 4 N HCl (12 h). The acidified samples were then filtered, on a 0.45-µm nitrocellulose paper and an excess of 250 g.l^{-1} of $BaCl_2$ solution was added to the filtrate to precipitate $BaSO_4$. After centrifugation, the barium

14

346   sulfate precipitate was washed several times with deionized distilled water and dried at 60°C

347   for 24 hours in an oven. $\delta^{34}S$ measurements were performed at the Biogéosciences Laboratory,

348   Dijon, France, on SO_2 molecules via combustion of ~500 µg of barium sulfate

349   homogeneously mixed with 1/3 of vanadium pentoxyde using a Vario PYRO cube (Elementar

350   GmbH) connected online via an open split device to an IsoPrime IRMS system (Isoprime,

351   Manchester, UK). International standard NBS 127 was used for calibration assuming a $\delta^{34}S$

352   value of +20.3‰ on the VCDT scale. Isotope results are reported in the standard delta

353   notation against the Vienna Cañon Diablo Troilite standard (VCDT). Analytical

354   reproducibility was better than ± 0.3‰ (1σ) based on replicates for standard materials.

355

356   *3.4. Major and trace elements*

357   Major and trace elements analyses were performed on selected samples by ICP-MS at

358   the Activation Laboratory (Actlabs) in Ancaster, Canada. The method used is Lithium

359   Metaborate/Tetraborate Fusion ICP and ICP-MS. Reproducibility was estimated by seven

360   replicate analyses of laboratory standards, and is better than 2% (1σ) for major and trace

361   elements.

362

363   *3.5. Petrographic observations*

364   Photonic observations of Mineral Mountains samples were performed using a Leica

365   MZ205c at the Biogéosciences Laboratory, Dijon. High-resolution images were obtained with

366   a JEOL JSM 6400F Field Emission SEM equipped with an Oxford INCA Energy 300 X-ray

367   Energy Dispersive Spectrometer (EDS) system for all chemical analyses at the ARCEN

368   platform (Laboratory Institut Carnot de Bourgogne in Dijon, Université de Bourgogne,

369   France). The thin sections were prepared for SEM analyses and were subsequently coated

370   with ~10 nm of graphite using a High Resolution Ion Beam Coater GATAN 681. The high-

371 resolution images were taken in back-scatter electron imaging mode to enhance the

372 compositional contrast. These facilities were used to identify rock textures and to examine

373 pyrite morphologies in samples from the studied section.

374

375 **4. Results and discussion**

376 *4.1. Carbonate carbon isotopes*

377 Except for samples MI169, MI197, MI202 and MI209, the $\delta^{13}C_{carb}$ values presented in

378 this work have already been reported in Thomazo et al. (2016). All data are consistent with

379 the expected $\delta^{13}C_{carb}$ decrease (by ~3‰) during the middle Smithian followed by an abrupt

380 increase (of ~4‰) through the late Smithian and the SSB (Fig. 3). Samples from the upper

381 part of unit A and from unit B (from 50.8 to 104.2 m) display a significant correlation of the

382 $\delta^{13}C_{carb}$ signal with the Mn content and Mn/Sr ratio (see figure 3 in Thomazo et al., 2016). In

383 this work, we also observe a covariation between the $\delta^{13}C_{carb}$ and the Mg/(Mg+Ca) ratios (Fig.

384 5). There is however no covariation between the $\delta^{13}C_{carb}$ and $\delta^{13}C_{org}$ signals at MI throughout

385 the units B, SSB and C (see figure 3 in Thomazo et al., 2016). Low $\delta^{13}C_{carb}$ values (~-3‰)

386 associated with high Mn/Sr and high Mg/(Mg+Ca) ratios are interpreted to reflect early

387 diagenetic authigenic precipitation of dolomicrites within reducing, Mn-bearing, ^{12}C enriched,

388 fluids produced during the bacterially mediated degradation of OM close to the sediment

389 water interface (Gilleaudeau and Kah, 2013; Schrag et al., 2013; Thomazo et al., 2016).

390

391 *4.2. Major and trace elements*

392 The Mg/(Mg+Ca) ratio varies from 0.01 to 0.13 with a mean value of 0.04 ± 0.03 (1σ)

393 (Table 1). The units A and B exhibit high ratios of 0.05 ± 0.03 and 0.05 ± 0.02 (1σ),

394 respectively. The unit C displays the lowest Mg/(Mg+Ca) ratio with an average of 0.02 ± 0.01

395   (1σ). Mg/(Mg+Ca) ratios decrease within the unit SSB (Fig. 3) and most likely provide a

396   direct record of the relative amount of dolomicrite versus carbonates in the samples. Indeed,

397   the carbonate concentration is strongly correlated to the sum of Ca plus Mg contents (Fig. 6, r

398   = +0.90, p < 0.01, n = 32).   The dolomitization most likely occurred early in the studied

399   section leading to the formation of nano to micro-meter-sized granular structures, poorly

400   preserved spherical dolomite and euhedral rhombs (Fig. 7A, 7B and 7C). Dolomite is often

401   observed in association with sheet-like mat and microbial structures. The formation of these

402   morphologies and structures has been interpreted as reflecting, microbially mediated, early

403   precipitation of dolomites (Lin et al., 2017) and their evolution into crystalline dolomite may

404   be explained by subsequent burial diagenesis (Rodriguez-Blanco et al., 2015).

405   The Mn/Sr ratio varies from 0.2 to 12.4 with a mean value of 2.2 ± 3.2 (1σ) (Table 1).

406   The units A and C show the smallest ratios with average values of 0.9 ± 0.6 and 1.1 ± 0.8 (1σ),

407   respectively, whereas units B and SSB display highest ratios with respective average values

408   of 6.8 ± 4.4 and 6.0 ± 8.0. Samples MI97 to MI127 (from 56 to 107.7 m), encompassing the

409   units B, SSB and the lowermost samples of the unit C (Fig. 3) show Mn/Sr values > 2. Due to

410   the high responsiveness of the Mn/Sr ratio to record reducing fluids during diagenesis

411   (Kaufman and Knoll, 1995), samples with Mn/Sr > 2 are considered here to have undergone

412   significant water-rock interactions during early diagenetic secondary processes (Pakhomova

413   et al., 2007; Thomazo et al., 2016).

414   Sulfur sulfide concentrations vary throughout the section, from 15 to 1329 ppm with a

415   mean value of 216 ± 301 ppm (1σ) (Table 1). These concentrations vary over a short time

416   scale and a well-defined trend across sedimentary deposits is not recognized. The Unit A

417   shows the strongest variations encompassing the total range of values, with a mean value of

418   163 ± 339 ppm (1σ). The microbial deposits from unit A are remarkably poor in sulfides

419   (only 48 ± 25 ppm; 1σ) compared to calcarenite and siltstones from the same unit or samples

420   from overlying units. Unit B shows the highest mean value, 474 ± 290 ppm (1σ), while the

421   unit SSB exhibits the lowest mean value, 131 ± 124 ppm (1σ). Concentrations in the unit C

422   are similar to those of the unit A, with a mean value of 206 ± 257 ppm (1σ).

423   Only nine samples yielded enough materials for CAS quantification of sulfate contents.

424   The concentrations vary from 23 to 72 ppm with a mean value of 35 ± 17 ppm (1σ). This

425   dataset is restricted and we did not attempt to outline any special trend along the section.

426   The TOC concentrations show variations from 0.02 to 0.37 wt. % with a mean value

427   of 0.114 ± 0.099 wt. % (1σ) (Fig. 3, Table 1). Units B, SSB and C exhibit similar TOC

428   concentrations with average values of 0.09 ± 0.04, 0.06 and 0.06 ± 0.02 wt. % (1σ),

429   respectively. Strongest variations in TOC content are observed in unit A and encompass the

430   highest mean value: 0.169 ± 0.115 wt. % (1σ). Within this unit, the microbial deposits show a

431   lower TOC concentration (0.04 ± 0.026 wt. %; 1σ) than the overlying calcarenite and

432   siltstones (0.218 ± 0.094 wt. %; 1σ). A clear maximum in TOC content is documented atop

433   the unit A, between MI72a and MI83 (Fig. 3). This maximum is associated with a negative

434   carbon isotope shift in $\delta^{13}C_{carb}$ (Fig. 3) and $\delta^{13}C_{org}$ values (down to -30.46‰; Thomazo et al.,

435   2016). Given the shallow depositional settings and the absence of evidence for anoxia in the

436   water column (Vennin et al., 2015; Thomazo et al., 2016), these features may be interpreted

437   as corresponding to a major perturbation of the global carbon cycle. It can result from a CO_2

438   released from volcanogenic (Sobolev et al., 2011) or thermogenic sources (Payne and Kump,

439   2007). However, changes in productivity and preservation of organic matter (i.e. the

440   biological pump) due to increasing temperatures (Fig. 3; Sun et al., 2012; Romano et al.,

441   2013) or changes in the relative contribution of the TOC between terrestrial and marine OM

442   (Caravaca et al., 2017a) may also explain this signal.

443   The S/C ratio fluctuates from 0.02 to 1.56 with a mean value of 0.38 ± 0.45 (1σ) (Fig.

444   3, Table 1). Units B, SSB and C show the highest ratios with values of 0.69 ± 0.37, 0.36 and

445   0.69 ± 0.36 (1σ), respectively. Excluding MI83 (S/C = 0.74; similar to values observed in

446   units B, SSB and C), unit A displays the lowest ratios with a mean of 0.07 ± 0.36 (1σ). S/C

447   ratio fluctuations in the units B, SSB and C are controlled by variations in the S content,

448   whereas unit A samples (except MI83) do not exhibit any covariation with either the TOC or

449   S content. The behavior of the sulfur and carbon contents through the section suggest that the

450   activity of microbial sulfate reduction (MSR) activity and ensuing sulfur sulfide precipitations

451   were probably not limited by sedimentary OM availability.

452

453   *4.3. Sulfide MSI results*

454   The $\delta^{34}S_{py}$ signal of sedimentary pyrites is highly variable with values ranging from -

455   21.2‰ to +46.7‰ (Fig. 3, Table 1). Positive values are recorded in units A, SSB and C. The

456   unit A shows positive, little variable, $\delta^{34}S_{py}$ values with an average isotopic composition of

457   12.2 ± 5.0‰ (1σ). The unit B documents strictly negative $\delta^{34}S_{py}$ values with an average

458   isotopic composition of -14.2 ± 6.8‰ (1σ). SSB samples yield positive $\delta^{34}S_{py}$ values of

459   +22.9‰ and +4.2‰. The unit C exhibits mostly positive $\delta^{34}S_{py}$ values but cover an extended

460   range of values (-3.0‰ to 46.7‰) with short time scale variations (mean $\delta^{34}S_{py}$ is 4.5 ±

461   16.4‰; 1σ; Fig. 3).

462   Overall, the $\Delta^{33}S_{py}$ signal varies from -0.01‰ to +0.12‰ with an average value of

463   0.05 ± 0.04‰ (1σ) (Fig. 3, Table 1). At its base, unit A shows values close to zero with an

464   average isotopic composition of 0.02 ± 0.03‰ (Table 1, Fig. 3). More positive values are

465   recorded in units B, SSB and C with average values of 0.08 ± 0.03‰, 0.06 ± 0.00‰ and 0.06

466   ± 0.04‰ (1σ), respectively. Small-scale variations of the $\Delta^{33}S_{py}$ signal (from 0.00‰ to

467   0.12 ‰) are recorded in unit C between 139.2 m and 148.3 m (Fig. 3). In this section, there is

468   no evidence of secondary hydrothermal or metamorphic alteration of the MSI record based on

469   petrographic observations of the samples. Instead, the lack of covariation between the $\delta^{34}S_{py}$

470   and sulfides content in all units (Table 1) and the observation of pyrite (FeS_2) in the form of

471   framboids suggest that microbial sulfur cycling had a dominant role on the $\delta^{34}S_{py}$ signal,

472   rather than the influence of secondary processes such as thermochemical sulfate reduction

473   (Machel et al., 1995).

474

475   *4.4. Interpretations of the sulfide MSI signal*

476   Most previous studies focusing on the Smithian-Spathian transition considered the

477   oceanic sulfur cycle under a steady state hypothesis where sulfides are precipitated after MSR

478   under open-system conditions (here defined as oceanic sulfate supply > microbial sulfate

479   reduction). However, at Mineral Mountains, this hypothesis cannot account for the high-

480   magnitude (from -21.2‰ to +46.7‰) and rapid (probably ≪50 kyr; see Brühwiler et al.,

481   2010) swings in $\delta^{34}S_{py}$ values between the units A and B and between units B and SSB. The

482   most positive $\Delta^{33}S_{py}$ values (up to +0.12‰) are also significantly above expected $\Delta^{33}S_{py}$ under

483   a steady state approximation (Wu et al., 2010). Instead, we suggest here that the observed

484   high-magnitude and rapid swings in $\delta^{34}S_{py}$ values can reflect deviations from the canonical

485   Phanerozoic $\delta^{34}S_{py}$ value (-20‰) produced under steady state open-system conditions (as

486   observed in unit B) to either (i) a Rayleigh-type distillation of the residual pore water sulfate

487   pool, or (ii) a partial or complete re-oxidation of the reduced sulfur pools produced during

488   MSR (units A, SSB and C) (see Fike et al., 2015 and references therein). Taking into account

489   the positive $\delta^{34}S_{py}$ values in units A, SSB and C, hypotheses (i) and (ii) have fundamentally

490   different paleoenvironments implications. If a Rayleigh distillation drove increasing $\delta^{34}S_{py}$

491   values, this implies that the residual sulfate pool might have evolved during the course of

492   sulfate reduction in a closed system with a disconnection between the pore water and the

overlying seawater (Fike et al., 2015). On the contrary, pyrites with heavy $\delta^{34}S$ that precipitated in shallow marine settings characterized by frequent and repeated abiotic oxidative reworking due to physical (e.g., through storm or tide activity) or biological (e.g. bioturbation) mixing of sediments can be produced during abiotic oxidation of sulfides (fractionation up to 5‰; Fry et al., 1988). The pyrite ^{34}S enrichment is in this case controlled by unsteady diagenetic processes and primarily reflects the efficiency of solute diffusion (pumping) and re-precipitation (refluxing) in the suboxic zone (Aller et al., 2008, 2010; Gao et al., 2013). Transport conditions and sedimentary dynamics indeed play a major role on the observed sulfur isotope pattern by promoting exchanges of sulfur and iron pools between the reduced deep layers and oxidized surface layers of unconsolidated sediments as shown in both the modern (Aller et al., 2010) and the geological sedimentary record (Pasquier et al., 2017). This process can result in geochemical records that preserve small or negative isotopic offsets between sulfate and sulfide (Sansjofre et al., 2016); these differences can be substantially less than the isotopic fractionation associated with microbial sulfur cycling in sediments (Fike et al., 2015). Finally, observed swings in $\delta^{34}S_{py}$ values can also reflect variations in the fractionation with reduced MSR ε^{34} associated with lowering sulfate concentrations or increasing cell-specific reduction rates (Leavitt et al., 2013).

In order to discriminate among these mechanisms, the use of the minor isotope of sulfur (^{33}S) in combination with the $\delta^{34}S_{py}$ signal has been previously successfully applied to various Phanerozoic sediments by some authors (e.g. Shen et al., 2011; Zhang et al., 2015, 2017; Saitoh et al., 2017). MSI analyses were first applied to the EPME context by Shen et al. (2011). They analyzed carbonate rocks across the PTB at the GSSP Meishan section, South China and based on a negative $\Delta^{33}S_{py}$ shift, they suggested that the episodic shoaling of anoxic deep-water caused the EPME. Recently, Zhang et al. (2015) analyzed the quadruple sulfur isotopic composition of carbonates across the end-Guadalupian extinction from two

518   sections in South China. They also suggested that the shoaling of sulfidic deep-waters

519   contributed to this extinction based on negative $\Delta^{33}S_{py}$ signatures. Both studies interpreted

520   negative $\Delta^{33}S_{py}$ signals as indicating the mixing of ^{34}S-enriched and ^{34}S-depleted sulfur from

521   two different sources. The shutdown of bioturbation in the sediments caused by shoaling of

522   toxic (anoxic/sulfidic) deep-waters was put forward to support this interpretation. However,

523   this inference was challenged by Saitoh et al. (2017). Based on an additional MSI record of

524   the end-Guadalupian event at Choatian, China, these authors proposed that in shallow marine

525   limestones deposited in oxic conditions, a negative $\Delta^{33}S_{py}$ shift can be also recorded and

526   reflects the mixing of two distinct types of pyrites precipitating from MSR in an open and

527   closed system. They subsequently suggested that bioturbation at Chaotian promoted MSR and

528   enhanced pyrite burial within the sediments. Thus, while these studies both agreed on the

529   mixing of different pools of sulfides to account for observed negative $\Delta^{33}S_{py}$ shifts, the link

530   with the bioturbation intensity and ensuing redox conditions was interpreted in opposite ways.

531   In the frame of these previous works, we report here the first MSI record across the

532   Smithian and the SSB (Fig. 8). The measured MSI correlate remarkably with the

533   lithostratigraphic units of the Mineral Mountains section and its $\delta^{13}C_{carb}$ record (Fig. 3). We

534   notably document steadily high $\Delta^{33}S_{py}$ values associated with low negative $\delta^{34}S_{pyr}$ in unit B,

535   while unit A shows low $\Delta^{33}S_{py}$ values associated with positive $\delta^{34}S_{py}$. In the units SSB and C,

536   the $\Delta^{33}S_{py}$ signal remains high and is associated with positive $\delta^{34}S_{py}$. Strong small-scale

537   fluctuations of the MSI signal are recorded in the unit C (Fig. 3).

538   *In vitro* laboratory experiments have shown that the MSI values of hydrogen sulfide

539   produced during MSR under non-limiting sulfate conditions is higher in $\Delta^{33}S_{py}$ and lower in

540      $\delta^{34}S_{py}$ compared to the substrate (Johnston et al., 2007; Sim et al, 2011a, 2011b). Therefore,

541   the high $\Delta^{33}S_{py}$ values associated with low negative $\delta^{34}S_{py}$ values of unit B (data in quadrant II

of figure 8) relative to contemporaneous seawater sulfate estimated by model calculation (Wu

et al., 2010) is consistent with sulfate reduction in an open system (i.e. sulfate supply > sulfate

reduction) with respect to sulfate. This is supported by evidence that most sulfides of unit B

are small pyrite framboids (Fig. 7C) congruent with MSR activity. Moreover, the likely

absence of an anoxic water column (Thomazo et al., 2016) and the abundant occurrences of

bioturbations and storm events (Figs. 3, 7A) recorded during the deposition of the unit B

suggest that pyrites precipitated synsedimentarily and that sediments were continuously

replenished in sulfates. In other words, the connectivity of the sedimentary pore water, where

MSR proceeded with the overlying water column, was probably strong during the deposition

of unit B. This MSI signal corresponds to an open system sulfate reduction. We hypothesize

that this connection was favored by a sustained sedimentary remobilization. Additionally, we

estimate that sulfur isotope fractionations during MSR in the unit B of Mineral Mountains

reflect values of $^{34}\varepsilon$ and $^{33}\lambda$ of 44.8‰ and 0.512, respectively, based on the sedimentary

sulfides and seawater sulfate isotopic compositions proposed by Wu et al. (2010; Fig. 8).

The $\delta^{34}S_{py}$ values of the unit SSB and most of unit C show highly positive values

associated with positive $\Delta^{33}S_{py}$ (Fig. 3, Table 1). These data mostly occurred in the quadrant I

of the figure 8 and fall above the regression line expected during open-system MSR.

Therefore, these positive $\delta^{34}S_{py}$ and $\Delta^{33}S$ values cannot be solely explained by variations in

MSR (a decrease in the MSR fractionation being accompanied by a decrease in the $\Delta^{33}S$

signal; Bradley et al., 2016) or sulfur disproportionation activities (Shen et al., 2011; Sim et

al., 2015; Zhang et al., 2015). In order to infer potential underlying mechanisms, we

superimposed on figure 8 (i) the mixing line of the sedimentary sulfide and seawater sulfate

endmembers, as well as the expected isotopic compositions of accumulative sulfides

produced during sulfate reduction in a closed system. Arrows in figure 8 show the evolution

of the residual sulfate and instantaneous sulfides during a closed-system Rayleigh distillation.

567   Isotopic data from the unit SSB and the lower part of unit C are largely consistent with the

568   range of values in a closed system Rayleigh distillation (including the mixing line between

569   accumulative sulfides and open system sulfides, Fig. 8). Importantly, they cannot be

570   explained by the mixing of sulfides produced during sulfate reduction in an open system and

571   produced during quantitative sulfate reduction in a closed system. Moreover, very highly ^{34}S-

572   enriched (and positive $\Delta^{33}S_{py}$) sulfides in parts of units SSB and C may reflect (i) the

573   evolution of the residual sulfate reservoirs from which sulfides precipitated and subsequent

574   MSR, or (ii) the precipitation of super heavy pyrite (i.e., $\delta^{34}S_{py} > \delta^{34}S_{CAS}$). Both of these

575   hypotheses are in accordance with a closed-system Rayleigh distillation model. However, we

576   cannot fully exclude here that the heaviest pyrite signal also reflect an H_2S pool produced

577   under low sulfate concentration, where some of the H_2S would have been partially oxidized

578   under aerobic conditions with an attendant effect resulting in sulfate that is lighter than the

579   H_2S available for capture as pyrite (Ries et al., 2009). Further analyses using secondary-ion

580   mass spectrometry will help to better address cumulative *versus* instantaneous isotopic effects

581   associated with these processes in a future study. The sulfides of the units SSB and C are

582   pyrite framboids of various sizes (Figs. 7E and 7F) consistent with MSR activity. According

583   to the record of trace elements (Thomazo et al., 2016), these sediments were deposited under

584   oxic conditions. A collapse in bioturbation and storm event occurrences are visible during the

585   late Smithian and at the SSB (Figs. 2, 5D). We therefore suggest that pyrites of unit SSB and

586   C precipitated synsedimentarily in pore water with a limited sulfate availability due to a rapid

587   disconnection of top-layer sediments with the overlying seawater sulfate reservoir. Such a

588   marked change may result from the absence of bioturbations at that time (see stratigraphic

589   variations of bioturbation intensity in, Fig. 3 and illustration of non-biotic and non-

590   bioturbated mudstones from the SSB unit in, Fig. 7D). This disappearance was coeval to, and

591   could have been a consequence of, the global late Smithian event, which for instance

592　corresponds to a major diversity loss in nektonic organisms (e.g., Brayard et al., 2009; Jattiot

593　et al. 2016). It may have also been generated by a strong increase in the sedimentation rate

594　(Pasquier et al., 2017), as observed regionally during the SSB and lower Spathian (Caravaca

595　et al., 2017b).

596　　　　Finally, most of the samples from the unit A show MSI values in-between quadrant I

597　and IV of figure 8, close to, or aligned with, the mixing line between two different pools (^{34}S-

598　enriched and ^{34}S-depleted sulfur) of pyrites precipitating from MSR in an open and closed

599　systems. In this case, when MSR occurs in an open system with respect to sulfates, pyrites

600　with substantially low $\delta^{34}S_{py}$ and high $\Delta^{33}S_{py}$ values are formed. In contrast, when sulfate

601　reduction goes to completion in a closed system, the sulfates are fully reduced and the $\delta^{34}S_{py}$

602　and $\Delta^{33}S_{py}$ values of the precipitated pyrites become equal to those of sulfates (Shen et al.,

603　2011; Sim et al., 2015; Zhang et al., 2015; Saitoh et al., 2017). The unit A samples are mainly

604　composed of dolomicrites and microbial limestones deposited in very shallow water

605　environments (Fig. 3). Burrows observed in the unit A may indicate that bioturbation activity

606　supplied sulfates into the limestone deposits and promoted MSR leading to the low $\delta^{34}S_{py}$ and

607　high $\Delta^{33}S_{py}$ values. However, the TOC in unit A is largely higher than in the unit B. The

608　sulfate reduction rate in the unit A may have been even higher than in unit B and perhaps also

609　to the rate of diffusive sulfate supply into the sediments due to the large amount of available

610　OM (Ohmoto, 1992; Ohmoto and Goldhaber, 1997) promoting "seawater sulfate like" $\delta^{34}S$

611　and $\Delta^{33}S$ values. Therefore, the observed variations in the $\delta^{34}S_{py}$ and $\Delta^{33}S_{py}$ values in unit A

612　probably better reflect the rate of mixing between the two types of pyrites. Because unit A

613　contained microbial limestones and dolomicrites corresponding to the development of

614　complex microbial ecosystems with the possible involvement of microbial sulfide oxidizers,

615　the processes that led to its MSI signal may also have been more complex by involving

25

616   several cycles of oxidation-reduction reactions (e.g., Canfield and Farquhar, 2009; Zerkle et

617   al., 2009, 2016; Johnston, 2011; Fike et al., 2015).

618

619   *4.5. CAS sulfur isotopes results*

620   Only nine samples over the twenty initially selected as part of this study yielded

621   enough material for CAS isotopic analyses. Results are therefore not subdivided with respect

622   to units of the studied section. No temporal trend can be documented. The $\delta^{34}S$ values of CAS

623   vary between +19.5‰ and +34.8‰ (mean value of +25.9 ± 6.3‰, 1σ) (Fig. 3, Table 1).

624   Results indicate a strong relationship between $\delta^{34}S_{CAS}$ and the Mg/(Mg+Ca) ratio (r = -0.64, p

625   = 0.06, n = 9, including all samples but increasing to r = -0.84, p < 0.01, n = 8, without MI163,

626   Fig. 9A), and between the $\delta^{34}S_{CAS}$ and the Mn/Sr ratio (r = -0.75, p < 0.02, n = 9, Fig. 9B).

627   Limestones with low Mg/(Mg+Ca) ratios show $\delta^{34}S_{CAS}$ of around +35‰, whereas

628   dolomicrites with high Mg/(Mg+Ca) ratios exhibit ^{32}S-enriched sulfur isotope compositions

629   around +20‰. There are no significant correlations between $\delta^{34}S_{CAS}$ and carbonate

630   concentration, $\delta^{13}C_{carb}$, $\delta^{34}S_{py}$ and CAS concentrations (Table 1).

631

632   *4.5. Fidelity and comparisons with other documented $\delta^{34}S$ signals from the Smithian-Spathian*

633   *transition.*

634   The observed range of $\delta^{34}S_{CAS}$ values are in agreement with previous measurements

635   from Spathian strata of the Moenkopi Formation, in the southernmost part of the SFB, that

636   yield values between +25‰ and +38‰ (Marenco et al., 2008), and more generally with most

637   Spathian sulfate $\delta^{34}S$ values falling between +25‰ and +30‰ VCDT (e.g., Cortecci et al.,

638   1981; Holser, 1984; Holser and Magaritz, 1987; Holser et al., 1988; Strauss, 1997; Luo et al.,

639   2010; Song et al., 2014b). Highly ^{34}S-enriched sulfates are characteristic of the Early Triassic

640   with maximum values of about +35‰ compared with values of ~+10‰ in the late Permian

641   (Holser et al., 1977; Claypool et al., 1980; Cortecci et al., 1981; Wilgus, 1981; Scholle, 1995;

642   Strauss, 1997; Kampschulte and Strauss, 2004; Longinelli and Flora, 2010; Song et al.,

643   2014b). However, the exact timing of the positive +35‰ maximum during the Early Triassic

644   differs from study to study with some authors suggesting that this maximum is restricted to

645   the Spathian (Wilgus, 1981; Marenco et al., 2008) or occurs across or immediately above the

646   PTB (Newton et al., 2004; Gorjan et al., 2007; Luo et al., 2010; Horacek et al., 2010; Song et

647   al., 2014b). Interestingly, some of the Early Triassic $\delta^{34}S_{CAS}$ records show large and rapid

648   variations within a section (Newton et al., 2004; Riccardi et al., 2006; Luo et al., 2010; Song

649   et al., 2014b). These behaviors have been interpreted to reflect a drawdown in seawater

650   sulfate concentration associated with a shortened residence time. Coupled variations in the

651   carbon and sulfur cycles are suggested and might be traced back using the $\delta^{13}C$ and $\delta^{34}S$

652   records when such paleoenvironmental conditions developed. Covariations between $\delta^{13}C$ and

653    $\delta^{34}S$ signals during periods of low seawater sulfate concentration have been hypothesized for

654   the Early Triassic in South China (Luo et al., 2010; Song et al., 2014b), but also during the

655   Paleozoic (Gill et al, 2007; Gill et al., 2011) and the Cretaceous (Adams et al., 2010). Such a

656   relationship between the $\delta^{34}S_{CAS}$ and $\delta^{13}C_{carb}$ signals cannot be identified in our dataset.

657   Several authors postulated that a gradient in sulfate $\delta^{34}S$ potentially developed within

658   water column depth during the Early Triassic (Newton et al., 2004; Kump et al., 2005;

659   Riccardi et al., 2006; Marenco, 2007). The advection of deep ^{34}S-enriched sulfate water

660   masses that formed during periods of prolonged global deep-ocean anoxia into shallow water

661   environments may explain variable sulfate $\delta^{34}S$ and deleterious biotic conditions due to

662   ensuing shallow marine euxinia (Isozaki, 1997; Newton et al., 2004; Grice et al., 2005; Kump

663   et al., 2005; Riccardi et al., 2006; Marenco, 2007). The observed stratigraphic variations in

664   Mg/(Mg+Ca) ratios (Fig. 3) and the negative correlation between the degree of dolomitization

665 and the $\delta^{34}S_{CAS}$ (Fig. 9A) suggest that the dolomitization process and associated $\delta^{34}S_{CAS}$ could

666 be facies-dependent, with shallowest sediments experiencing a higher degree of

667 dolomitization compared to deepest sediments. These observations are consistent with the

668 hypothesis of a gradient in sulfate $\delta^{34}S$, with the dolomitized samples recording the lower

669 $\delta^{34}S_{CAS}$. However, (i) a water column anoxia is not documented at Mineral Mountains and the

670 advection of anoxic water masses to the shallowest part of the SFB is not kinetically-

671 supported by the carbon isotopes record (Thomazo et al., 2016), and (ii) the relationships

672 observed between the $\delta^{34}S_{CAS}$ and both Mg/(Mg+Ca) and Mn/Sr ratios (Fig. 9A and 9B)

673 indicate that the sulfur isotope signal of CAS mostly reflects variations in early diagenetic

674 processes including the degree of dolomitization. Accordingly, we postulate that only samples

675 exhibiting Mn/Sr below 0.5 record primary CAS-derived $\delta^{34}S$ sulfate with values between

676 +32.4‰ and +34.8‰. This approximation is in agreement with the estimates by Marenco et al.

677 (2008) interpreting a weaker altered signal in the Moenkopi Formation of the southern SFB,

678 which exhibits sulfate $\delta^{34}S$ values between +31‰ and +38‰.

679 Nevertheless, several early diagenetic reactions associated with secondary fluids can

680 be deduced from the $\delta^{34}S_{CAS}$ record at Mineral Mountains. Indeed, during early diagenesis,

681 the MSR activity tends to produce a ^{34}S-enriched CAS record (Marenco et al., 2008),

682 especially if reduction occurred under a Rayleigh-type distillation in a closed system with

683 respect to sulfates, as deduced from the MSI signal in samples from units SSB and C (Fig. 8).

684 However, because OM fuels MSR a positive relationship between TOC and $\delta^{34}S_{CAS}$ and an

685 increasing S/C ratio associated with ^{34}S-enriched CAS might be expected (Raiswell and

686 Canfield, 2012). No such relationship between the $\delta^{34}S_{CAS}$ and TOC or between the $\delta^{34}S_{CAS}$

687 and S/C can be documented using our restricted available data set.

688 In the unit C (between MI159 and MI169) significant small-scale $\delta^{34}S_{CAS}$ variations

689 (15‰ in amplitude) are also observed independently of the TOC, S/C ratio and paired $\delta^{34}S$ of

690   pyrites. Such high-frequency fluctuations of the $\delta^{34}S_{CAS}$ signal are difficult to explain by

691   secular variations in seawater sulfate sulfur isotopic composition in a steady-state global

692   sulfur cycle. Indeed, these variations are much more rapid ($\ll$50 kyr, Brühwiler et al., 2010)

693   than the sulfate residence time in the ocean (i.e., 13 Myr in the modern ocean, Kah et al.,

694   2004; but probably reduced to 1.3 Myr during the Triassic due to lower sulfate concentration,

695   Horita et al., 2002). Rapid changes of the $\delta^{34}S_{CAS}$ signal during the Griesbachian to Smithian

696   interval have nonetheless been interpreted to reflect very low sulfate concentrations ($\leq$4 mM)

697   with a residence time of oceanic sulfate reduced to $\leq$200 kyr (Song et al., 2014b). Thus, a

698   partial influence of a global signal cannot be completely discarded in our case.

699   Finally, the strong correlation between the $\delta^{34}S_{CAS}$ and the degree of dolomitization

700   and the Mn/Sr ratio, as well as the identification of a closed system Rayleigh-type distillation

701   of sulfur species, makes a compelling case for synsedimentary early diagenetic processes as

702   the main control for the CAS sulfur isotope signal observed at Mineral Mountains.

703

704   **5. Perspectives on the use of MSI record in its sedimentological context**

705   The Mineral Mountains MSI signal is slightly different from previous observations for

706   the sedimentary sulfur cycle associated with bioturbation during the Phanerozoic. In Shen et

707   al. (2011), negative sulfide $\Delta^{33}S$ values measured across the PTB were suggested to reflect the

708   mixing of two types of pyrite formed during both an open system and a quantitative closed

709   system MSR. Shen et al. (2011) linked this mixing to a shutdown of bioturbation resulting

710   from the shoaling of anoxic deep waters that led to the EPME. According to this model, the

711   pore water exchanged continuously with oceanic sulfate under oxic conditions because of the

712   enhanced bioturbation (associated with low $\delta^{34}S$ and high $\Delta^{33}S$). On the contrary, bioturbation

713   would have disappeared during anoxia and the sulfate supply into sediments was suppressed,

714   leading to quantitative pore water sulfate reduction (high $\delta^{34}S_{py}$ and low $\Delta^{33}S_{py}$). A similar

715   scenario was proposed by Zhang et al. (2015), who interpreted negative $\Delta^{33}S$-$\delta^{34}S$ values of

716   pyrites around the PTB as corresponding to pyrites produced in a shoaling sulfidic water

717   column. More recently, these interpretations have been challenged by Saitoh et al. (2017)

718   based on the MSI record across the Guadalupian-Lopingian (Late Permian) boundary at

719   Chaotian (China). They showed that the setting of pore water sediments under oxic conditions

720   are not always an open system with respect to sulfates, even if bioturbation is associated.

721   Therefore, the development of anoxic conditions and consequent shutdown of bioturbation are

722   not required to produce negative $\Delta^{33}S_{py}$ values and processes linking the sedimentary sulfur

723   cycle to bioturbation are more complicated than previously thought.

724   Contrasting with Saitoh et al. (2017) we established here (Fig. 8, Section 4.3) a strong

725   relationship between bioturbation and the MSI signal recorded within the permanently oxic

726   bottom water conditions that developed at Mineral Mountains across the SSB. Bioturbation,

727   which is a necessary driver to sustain intense iron and sulfur cycling in marine sediments

728   through the suboxic zone (Van de Velde et al., 2016), likely continuously supplied sulfates

729   into the sediments and stimulates the sulfate reduction and *in situ* sulfide precipitation in the

730   sediments during the deposition of the middle Smithian unit B. During this period, open

731   system MSR activity from pore water fluids connected to oceanic waters is in accordance

732   with (i) the higher average concentration of sulfides, (ii) the observation of pyrite (FeS_2) in

733   the form of framboids, and (iii) the MSI signatures. Moreover, unit B records low $\delta^{13}C_{carb}$

734   values associated with high Mn/Sr and high Mg/(Mg+Ca) ratios. Such variations are in

735   agreement with a strong influence of the MSR activity on the geochemistry of the sediments.

736   Indeed, MSR is well known for its role in promoting the precipitation of early diagenetic

737   authigenic carbonates and secondary carbonates such as dolostones with low $\delta^{13}C_{carb}$ values

738   through the consumption of excess protons (Vasconcelos and McKenzie, 1997; Zhang et al.,

739   2012; Thomazo et al., 2016), within reducing Mn-bearing, ^{12}C-enriched, fluids produced

740   during the bacterially mediated degradation of OM in the suboxic/anoxic zone.

741   On the contrary, during the deposition of both unit SSB and the lower part of unit C,

742   the disappearance of bioturbation (see stratigraphic variations of bioturbation intensity in Fig.

743   3 and illustration of non-biotic and non-bioturbated mudstones from the SSB unit in Fig. 7D), ,

744   may have strongly reduced the pore water replenishment in sulfates, therefore leading to; (i)

745   reduced *in situ* sulfide precipitation, (ii) MSI signatures typical of a closed system Rayleigh-

746   type distillation, and (iii) reduced early diagenetic remineralization processes (i.e., lower

747   Mn/Sr and lower Mg/(Mg+Ca) ratios, higher $\delta^{13}C_{carb}$) due to the shortage in oxidant

748   availability.

749   The relationship between secular trends in bioturbation patterns and the sedimentary

750   geochemical signatures observed at Mineral Mountains, together with the absence of anoxia,

751   support the primary influence of local processes as an important driver of isotopic trends

752   observed before and across the SSB. Worldwide correlation of the Smithian-Spathian $\delta^{13}C$

753   signal (Fig. 1) is more easily explained by modifications of the global carbon cycle if the

754   primary driver of the muted $\delta^{13}C_{carb}$ and $\delta^{34}S_{py}$ signatures across the SSB reflects the collapse

755   of biogenic sediment mixing and subsequent changes in the connectivity of sedimentary pore

756   waters with the overlying water column. These have likely influenced the geochemical

757   properties of sediments over large distances and may have also generated a global pattern

758   (Hofmann et al., 2015; Pasquier et al, 2017). If these hypotheses are confirmed, they also

759   suggest that many commonly used proxies to infer Early Triassic seawater anoxia may rather

760   reflect the poor sediment oxygenation arising from the extinction of organisms performing

761   bioturbation.

762   Finally, the use of MSI geochemistry, together with strong sedimentological

763   constraints, show that changes in the sulfur cycle before and across the SSB at Mineral

Mountains is most probably a local consequence of the late Smithian extinction event rather than recording the development of a lethal global anoxic ocean. Therefore, the data reported in this study demonstrate that the sulfide MSI signal can be a valuable proxy for assessing local paleoenvironmental and sedimentological processes throughout Earth history.

6. Conclusions

The study of the multiple sulfur isotope records before and across the SSB at Mineral Mountains provides new insights into the Early Triassic sulfur cycle and its temporal and mechanistic relationships with local sedimentological conditions, the $\delta^{13}C$ curve variations and the decrease in diversity and abundance among benthic organisms. We notably show that:

1. The $\Delta^{33}S$-$\delta^{34}S$ signals reflect the operation of MSR in two different regimes. Before the late Smithian, open system sulfate reduction in sediments pore water connected to the seawater is prevailing, while during the late Smithian and after the SSB, a closed-system, sulfate-limited, Rayleigh-type distillation is recorded in the MSI signals.

2. No change in the oxygenation of the water column accompanied this evolution of the MSI record and all pyrite framboids formed in the sediment pore water were precipitated under an overlying oxygenated water column.

3. The connection of pore waters to the overlying water column is locally controlled by sedimentological conditions such as bioturbation intensity and sedimentation rate. This led to a constant replenishment in pore water sulfates during the middle Smithian, and an impoverishment during the late Smithian and across the SSB.

4. Both the C and S isotope signals at Mineral Mountains are therefore best explained by the extent to which MSR and associated early diagenetic remineralization proceeded within the sediments.

788   Finally, we suggest that the muted sulfur isotope record at Mineral Mountains is a

789 consequence of the late Smithian extinction and the associated loss of the sedimentary mixed

790 layer. Future isotopic studies on other sections across the SSB in various sedimentological

791 contexts should be used to further test in detail these inferences and help to improve our

792 understanding of the importance of local synsedimentary processes for paleoenvironmental

793 reconstructions during the EPME recovery and, more generally, over geological times.

794

803

804 **References**

805 Adams, D.D., Hurtgen, M.T., Sageman, B.B., 2010. Volcanic triggering of a biogeochemical
806 cascade during Oceanic Anoxic Event 2. Nature Geoscience 3, 201–204.
807 https://doi.org/10.1038/ngeo743

808 Algeo, T.J., Ellwood, B., Nguyen, T.K.T., Rowe, H., Maynard, J.B., 2007. The Permian–
809 Triassic boundary at Nhi Tao, Vietnam: Evidence for recurrent influx of sulfidic watermasses
810 to a shallow-marine carbonate platform. Palaeogeography, Palaeoclimatology, Palaeoecology
811 252, 304–327. https://doi.org/10.1016/j.palaeo.2006.11.055

812 Algeo, T., Shen, Y., Zhang, T., Lyons, T., Bates, S., Rowe, H., Nguyen, T.K.T., 2008.
813 Association of ^{34}S-depleted pyrite layers with negative carbonate δ^{13}C excursions at the
814 Permian-Triassic boundary: Evidence for upwelling of sulfidic deep-ocean water masses.
815 Geochemistry, Geophysics, Geosystems 9, n/a-n/a. https://doi.org/10.1029/2007gc001823

816 Algeo, T.J., Twitchett, R.J., 2010. Anomalous Early Triassic sediment fluxes due to elevated
817 weathering rates and their biological consequences. Geology 38, 1023–1026.
818 https://doi.org/10.1130/g31203.1

819 Algeo, T.J., Chen, Z.Q., Fraiser, M.L., Twitchett, R.J., 2011. Terrestrial–marine
820 teleconnections in the collapse and rebuilding of Early Triassic marine ecosystems.
821 Palaeogeography, Palaeoclimatology, Palaeoecology 308, 1–11.
822 https://doi.org/10.1016/j.palaeo.2011.01.011

823 Aller, R.C., Blair, N.E., Brunskill, G.J., 2008. Early diagenetic cycling, incineration, and
824 burial of sedimentary organic carbon in the central Gulf of Papua (Papua New Guinea).
825 Journal of Geophysical Research 113. https://doi.org/10.1029/2006jf000689

826 Aller, R.C., Madrid, V., Chistoserdov, A., Aller, J.Y., Heilbrun, C., 2010. Unsteady
827 diagenetic processes and sulfur biogeochemistry in tropical deltaic muds: implications for
828 oceanic isotope cycles and the sedimentary record. Geochim. Cosmochim. Acta 74, 4671–92.

829 Bau, M., Dulski, P., 1996. Distribution of yttrium and rare-earth elements in the Penge and
830 Kuruman iron-formations, Transvaal Supergroup, South Africa. Precambrian Research 79,
831 37–55. https://doi.org/10.1016/0301-9268(95)00087-9

832 Beatty, T.W., Zonneveld, J.-P., Henderson, C.M., 2008. Anomalously diverse Early Triassic
833 ichnofossil assemblages in northwest Pangea: A case for a shallow-marine habitable zone.
834 Geology 36, 771-774. https://doi.org/10.1130/g24952a.1

835 Berner, R.A., Raiswell, R., 1983. Burial of organic carbon and pyrite sulfur in sediments over
836 Phanerozoic time: a new theory. Geochimica et Cosmochimica Acta 47, 855-862.

837 Bottrell, S. H., Newton, R. J., 2006. Reconstruction of changes in global sulfur cycling from
838 marine sulfate isotopes. Earth-Science Reviews 75, 59-83.

839 Bradley, A. S., Leavitt, W. D., Schmidt, M., Knoll, A. H., Girguis, P. R., Johnston, D. T.,
840 2016. Patterns of sulfur isotope fractionation during microbial sulfate reduction. Geobiology
841 14, 91-101.

842 Brayard, A., Bucher, H., Escarguel, G., Fluteau, F., Bourquin, S., Galfetti, T., 2006. The Early
843 Triassic ammonoid recovery: Paleoclimatic significance of diversity gradients.
844 Palaeogeography, Palaeoclimatology, Palaeoecology 239, 374–395.
845 https://doi.org/10.1016/j.palaeo.2006.02.003

846 Brayard, A., Escarguel, G., Bucher, H., 2007. The biogeography of Early Triassic ammonoid
847 faunas: Clusters, gradients, and networks. Geobios 40, 749–765.
848 https://doi.org/10.1016/j.geobios.2007.06.002

849 Brayard, A., Brühwiler, T., Bucher, H., Jenks, J., 2009. *Guodunites*, a low-palaeolatitude and
850 trans-panthalassic Smithian (Early Triassic) ammonoid genus. Palaeontology 52, 471–481.
851 https://doi.org/10.1111/j.1475-4983.2009.00855.x

852 Brayard, A., Vennin, E., Olivier, N., Bylund, K.G., Jenks, J., Stephen, D.A., Bucher, H.,
853 Hofmann, R., Goudemand, N., Escarguel, G., 2011. Transient metazoan reefs in the aftermath

854   of the end-Permian mass extinction. Nature Geoscience 4, 693–697.
855   https://doi.org/10.1038/ngeo1264

856   Brayard, A., Bylund, K.G., Jenks, J.F., Stephen, D.A., Olivier, N., Escarguel, G., Fara, E.,
857   Vennin, E., 2013. Smithian ammonoid faunas from Utah: implications for Early Triassic
858   biostratigraphy, correlation and basinal paleogeography. Swiss Journal of Palaeontology 132,
859   141–219. https://doi.org/10.1007/s13358-013-0058-y

860   Brayard, A., Meier, M., Escarguel, G., Fara, E., Nützel, A., Olivier, N., Bylund, K.G., Jenks,
861   J.F., Stephen, D.A., Hautmann, M., Vennin, E., Bucher, H., 2015. Early Triassic Gulliver
862   gastropods: Spatio-temporal distribution and significance for biotic recovery after the end-
863   Permian mass extinction. Earth-Science Reviews 146, 31–64.
864   https://doi.org/10.1016/j.earscirev.2015.03.005

865   Brayard, A., Krumenacker, L.J., Botting, J.P., Jenks, J.F., Bylund, K.G., Fara, E., Vennin, E.,
866   Olivier, N., Goudemand, N., Saucède, T., Charbonnier, S., Romano, C., Doguzhaeva, L.,
867   Thuy, B., Hautmann, M., Stephen, D.A., Thomazo, C., Escarguel, G., 2017. Unexpected
868   Early Triassic marine ecosystem and the rise of the Modern evolutionary fauna. Science
869   Advances 3, e1602159. https://doi.org/10.1126/sciadv.1602159

870   Brosse, M., Brayard, A., Fara, E., Neige, P., 2013. Ammonoid recovery after the Permian–
871   Triassic mass extinction: a re-exploration of morphological and phylogenetic diversity
872   patterns. Journal of the Geological Society 170, 225–236. https://doi.org/10.1144/jgs2012-084

873   Brühwiler, T., Bucher, H., Brayard, A., Goudemand, N., 2010. High-resolution biochronology
874   and diversity dynamics of the Early Triassic ammonoid recovery: The Smithian faunas of the
875   Northern Indian Margin. Palaeogeography, Palaeoclimatology, Palaeoecology 297, 491–501.
876   https://doi.org/10.1016/j.palaeo.2010.09.001

877   Brunner, B., Bernasconi, S.M., 2005. A revised isotope fractionation model for dissimilatory
878   sulfate reduction in sulfate reducing bacteria. Geochim. Cosmochim. Acta 69, 4759–71.

879   Burchfiel, B.C., Davis, G.A., 1975. Nature and controls of Cordilleran orogenesis, western
880   United States: Extensions of an earlier synthesis. American Journal of Science 275, 363-396.

881   Burgess, S.D., Bowring, S., Shen, S., 2014. High-precision timeline for Earth's most severe
882   extinction. Proceedings of the National Academy of Sciences 111, 3316–3321.
883   https://doi.org/10.1073/pnas.1317692111

884   Canfield, D.E., Raiswell, R., Westrich, J.T., Reaves, C.M., Berner, R.A., 1986. The use of
885   chromium reduction in the analysis of reduced inorganic sulfur in sediments and shales.
886   Chemical Geology 54, 149–155. https://doi.org/10.1016/0009-2541(86)90078-1

887   Canfield, D.E., Thamdrup, B., 1994. The production of ^{34}S-depleted sulfide during bacterial
888   disproportionation of elemental sulfur. Science 266, 1973–75.

889   Canfield, D.E., Teske, A., 1996. Late Proterozoic rise in atmospheric oxygen concentration
890   inferred from phylogenetic and sulphur-isotope studies. Nature 382, 127–32.

891   Canfield, D.E., 2001. Biogeochemistry of sulfur isotopes. Reviews in Mineralogy and
892   Geochemistry 43, 607-636.

893   Canfield, D.E., Farquhar, J., 2009. Animal evolution, bioturbation, and the sulfate
894   concentration of the oceans. Proceedings of the National Academy of Sciences 106, 8123–
895   8127. https://doi.org/10.1073/pnas.0902037106

896   Canfield, D.E., Farquhar, J., Zerkle, A.L., 2010. High isotope fractionations during sulfate
897   reduction in a low-sulfate euxinic ocean analog. Geology 38, 415–18.

898   Caravaca, G., Thomazo, C., Vennin, E., Olivier, N., Cocquerez, T., Escarguel, G., Fara, E.,
899   Jenks, J.F., Bylund, K.G., Stephen, D.A., Brayard, A., 2017a. Early Triassic fluctuations of
900   the global carbon cycle: New evidence from paired carbon isotopes in the western USA basin.
901   Global and Planetary Change 154, 10–22. https://doi.org/10.1016/j.gloplacha.2017.05.005

902   Caravaca, G., Brayard, A., Vennin, E., Guiraud, M., Le Pourhiet, L., Grosjean, A.-S.,
903   Thomazo, C., Olivier, N., Fara, E., Escarguel, G., Bylund, K.G., Jenks, J.F., Stephen, D.A.,
904   2017b. Controlling factors for differential subsidence in the Sonoma Foreland Basin (Early
905   Triassic,   western   USA).   Geological   Magazine   1–25.
906   https://doi.org/10.1017/s0016756817000164

907   Chambers, L.A., Trudinger, P.A., Smith, J.W., Burns, M. S., 1975. Fractionation of sulfur
908   isotopes by continuous cultures of Desulfovibrio desulfuricans. Canadian Journal of
909   Microbiology 21, 1602-1607.

910   Clarkson, M.O., Richoz, S., Wood, R.A., Maurer, F., Krystyn, L., McGurty, D.J., Astratti, D.,
911   2013. A new high-resolution δ^{13}C record for the Early Triassic: Insights from the Arabian
912   Platform. Gondwana Research 24, 233–242. https://doi.org/10.1016/j.gr.2012.10.002

913   Clarkson, M.O., Wood, R.A., Poulton, S.W., Richoz, S., Newton, R.J., Kasemann, S.A.,
914   Bowyer, F., Krystyn, L., 2016. Dynamic anoxic ferruginous conditions during the end-
915   Permian   mass   extinction   and   recovery.   Nature   Communications   7,   12236.
916   https://doi.org/10.1038/ncomms12236

917   Claypool, G.E., Holser, W.T., Kaplan, I.R., Sakai, H., Zak, I., 1980. The age curves of sulfur
918   and oxygen isotopes in marine sulfate and their mutual interpretation. Chemical Geology 28,
919   199–260. https://doi.org/10.1016/0009-2541(80)90047-9

920   Collinson, J.W., Kendall, C.G.S.C., Marcantel, J.B., 1976. Permian-Triassic boundary in
921   eastern Nevada and west-central Utah. Geological Society of America Bulletin 87, 821.
922   https://doi.org/10.1130/0016-7606(1976)87<821:pbiena>2.0.co;2

923   Cortecci, G., Reyes, E., Berti, G., Casati, P., 1981. Sulfur and oxygen isotopes in Italian
924   marine   sulfates   of   Permian   and   Triassic   ages.   Chemical   Geology   34,   65–79.
925   https://doi.org/10.1016/0009-2541(81)90072-3

926   Cui, H., Kaufman, A.J., Xiao, S., Zhu, M., Zhou, C., Liu, X.-M., 2015. Redox architecture of
927   an Ediacaran ocean margin: Integrated chemostratigraphic (δ^{13}C–δ^{34}S–^{87}Sr/^{86}Sr–Ce/Ce*)
928   correlation of the Doushantuo Formation, South China. Chemical Geology 405, 48–62.
929   https://doi.org/10.1016/j.chemgeo.2015.04.009

930 Cui, H., Kaufman, A.J., Xiao, S., Zhou, C., Liu, X.-M., 2017. Was the Ediacaran Shuram
931 Excursion a globally synchronized early diagenetic event? Insights from methane-derived
932 authigenic carbonates in the uppermost Doushantuo Formation, South China. Chemical
933 Geology 450, 59–80. https://doi.org/10.1016/j.chemgeo.2016.12.010

934 Dagys A.S., 1988. Major features of the geographic differentiation of Triassic ammonoids. In:
935 Wiedmann J, Kullman J (eds) Cephalopods—Present and past. Schweizerbart, Stuttgart

936 Dickinson, W.R., 2013. Phanerozoic palinspastic reconstructions of Great Basin geotectonics
937 (Nevada-Utah, USA). Geosphere 9, 1384–1396. https://doi.org/10.1130/ges00888.1

938 Fike, D.A., Grotzinger, J.P., Pratt, L.M., Summons, R.E., 2006. Oxidation of the Ediacaran
939 ocean. Nature 444, 744–47.

940 Fike, D.A., Gammon, C.L., Ziebis, W., Orphan, V.J., 2008. Micron-scale mapping of sulfur
941 cycling across the oxycline of a cyanobacterial mat: a paired nanoSIMS and CARD-FISH
942 approach. ISME J. 2, 749–59.

943 Fike, D.A., Grotzinger, J.P., 2008. A paired sulfate–pyrite $\delta 34S$ approach to understanding
944 the evolution of the Ediacaran–Cambrian sulfur cycle. Geochim. Cosmochim. Acta 72, 2636–
945 48.

946 Fike, D.A., Finke, N., Zha, J., Blake, G., Hoehler, T.M., Orphan, V.J., 2009. The effect of
947 sulfate concentration on (sub)millimeter-scale sulfide $\delta 34S$ in hypersaline cyanobacterial mats
948 over the diurnal cycle. Geochim. Cosmochim. Acta 73, 6187–204.

949 Fike, D.A., Bradley, A.S., Rose, C.V., 2015. Rethinking the Ancient Sulfur Cycle. Annual
950 Review of Earth and Planetary Sciences 43, 593–622. https://doi.org/10.1146/annurev-earth-
951 060313-054802

952 Fry, B., Gest, H., Hayes, J.M., 1984. Isotope effects associated with the anaerobic oxidation
953 of sulfide by the purple photosynthetic bacterium, *Chromatium vinosum*. FEMS Microbiol.
954 Lett. 22, 283–87.

955 Fry, B., Ruf, W., Gest, H., Hayes, J.M., 1988. Sulfur isotope effects associated with oxidation
956 of sulfide by O_2 in aqueous solution. Chem. Geol. 73, 205–10.

957 Galfetti, T., Bucher, H., Ovtcharova, M., Schaltegger, U., Brayard, A., Brühwiler, T.,
958 Goudemand, N., Weissert, H., Hochuli, P.A., Cordey, F., Guodun, K., 2007a. Timing of the
959 Early Triassic carbon cycle perturbations inferred from new U–Pb ages and ammonoid
960 biochronozones. Earth and Planetary Science Letters 258, 593–604.
961 https://doi.org/10.1016/j.epsl.2007.04.023

962 Galfetti, T., Hochuli, P.A., Brayard, A., Bucher, H., Weissert, H., Vigran, J.O., 2007b.
963 Smithian-Spathian boundary event: Evidence for global climatic change in the wake of the
964 end-Permian biotic crisis. Geology 35, 291. https://doi.org/10.1130/g23117a.1

965 Galfetti, T., Bucher, H., Martini, R., Hochuli, P.A., Weissert, H., Crasquin-Soleau, S.,
966 Brayard, A., Goudemand, N., Brühwiler, T., Guodun, K., 2008. Evolution of Early Triassic
967 outer platform paleoenvironments in the Nanpanjiang Basin (South China) and their

968   significance for the biotic recovery. Sedimentary Geology 204, 36–60.
969   https://doi.org/10.1016/j.sedgeo.2007.12.008

970   Gao, J., Fike, D.A., Aller, R.C., 2013. Enriched pyrite δ^{34}S signals in modern tropical deltaic
971   muds. Presented at AGU Fall Meet., Dec. 9–13, San Francisco. Abstr. B31A-0352.

972   Garrels, R.M., Lerman, A., 1984. Coupling of the sedimentary sulfur and carbon cycles; an
973   improved model. American Journal of Science 284, 989–1007.
974   https://doi.org/10.2475/ajs.284.9.989

975   Gill, B.C., Lyons, T.W., Saltzman, M.R., 2007. Parallel, high-resolution carbon and sulfur
976   isotope records of the evolving Paleozoic marine sulfur reservoir. Palaeogeography,
977   Palaeoclimatology, Palaeoecology 256, 156–173.
978   https://doi.org/10.1016/j.palaeo.2007.02.030

979   Gill, B.C., Lyons, T.W., Young, S.A., Kump, L.R., Knoll, A.H., Saltzman, M.R., 2011.
980   Geochemical evidence for widespread euxinia in the Later Cambrian ocean. Nature 469, 80–
981   83. https://doi.org/10.1038/nature09700

982   Gilleaudeau, G.J., Kah, L.C., 2013. Carbon isotope records in a Mesoproterozoic epicratonic
983   sea: carbon cycling in a low-oxygen world. Precambrian Research 228, 85–101.

984   Gomes, M.L., Hurtgen, M.T., 2013. Sulfur isotope systematics of a euxinic, low-sulfate lake:
985   evaluating the importance of the reservoir effect in modern and ancient oceans. Geology 41,
986   663–66.

987   Gomes, M.L., Fike, D.A., Bergmann, K.D., Jones, C., Knoll, A.H., 2017. Environmental
988   insights from high-resolution (SIMS) sulfur isotope analyses of sulfides in Proterozoic
989   microbialites with diverse mat textures. Geobiology. https://doi.org/10.1111/gbi.12265

990   Gorjan, P., Kaiho, K., Kakegawa, T., Niitsuma, S., Chen, Z.Q., Kajiwara, Y., Nicora, A.,
991   2007. Paleoredox, biotic and sulfur-isotopic changes associated with the end-Permian mass
992   extinction in the western Tethys. Chemical Geology 244, 483–492.
993   https://doi.org/10.1016/j.chemgeo.2007.07.003

994   Grasby, S.E., Beauchamp, B., Embry, A., Sanei, H., 2013. Recurrent Early Triassic ocean
995   anoxia. Geology 41, 175–178. https://doi.org/10.1130/g33599.1

996   Grice, K., Cao, C., Love, G. D., Boettcher, M. E., Twitchett, R. J., Grosjean, E., Summons, R.
997   E., Turgeon, S. C., Dunning, W., Jin, Y., 2005. Photic Zone Euxinia During the Permian-
998   Triassic Superanoxic Event. Science 307, 706–709. https://doi.org/10.1126/science.1104323

999   Guex. J., Hungerbühler, A., Jenks, J.F., O'Dogherty, L., Atudorei, V., Taylor, D.G., Bucher,
1000 H., Bartolini, A., 2010. Spathian (Lower Triassic) ammonoids from western USA (Idaho,
1001 California, Utah and Nevada). Mémoires de Géologie de Lausanne, 49, 1-81.

1002 Habicht, K.S., Canfield, D.E., 1997. Sulfur isotope fractionation during bacterial sulfate
1003 reduction in organic-rich sediments. Geochim. Cosmochim. Acta 61, 5351–61.

1004   Habicht, K.S., Canfield, D.E., Rethmeier, J. 1998. Sulfur isotope fractionation during
1005   bacterial reduction and disproportionation of thiosulfate and sulfite. Geochim. Cosmochim.
1006   Acta 62, 2585–95.

1007   Haq, B.U., Hardenbol, J., Vail, P.R., 1987. Chronology of Fluctuating Sea Levels Since the
1008   Triassic. Science 235, 1156–1167. https://doi.org/10.1126/science.235.4793.1156

1009   Hermann, E., Hochuli, P.A., Méhay, S., Bucher, H., Brühwiler, T., Ware, D., Hautmann, M.,
1010   Roohi, G., ur-Rehman, K., Yaseen, A., 2011. Organic matter and palaeoenvironmental signals
1011   during the Early Triassic biotic recovery: The Salt Range and Surghar Range records.
1012   Sedimentary Geology 234, 19–41. https://doi.org/10.1016/j.sedgeo.2010.11.003

1013   Hofmann, R., Hautmann, M., Brayard, A., Nützel, A., Bylund, K.G., Jenks, J.F., Vennin, E.,
1014   Olivier, N., Bucher, H., 2014. Recovery of benthic marine communities from the end-Permian
1015   mass extinction at the low latitudes of eastern Panthalassa. Palaeontology 57, 547–589.
1016   https://doi.org/10.1111/pala.12076

1017   Hofmann, R., Buatois, L.A., MacNaughton, R.B., Mángano, M.G., 2015. Loss of the
1018   sedimentary mixed layer as a result of the end-Permian extinction. Palaeogeography,
1019   Palaeoclimatology, Palaeoecology 428, 1–11. https://doi.org/10.1016/j.palaeo.2015.03.036

1020   Holser, W.T., 1977. Catastrophic chemical events in the history of the ocean. Nature 267,
1021   403–408. https://doi.org/10.1038/267403a0

1022   Holser, W.T., 1984. Gradual and Abrupt Shifts in Ocean Chemistry During Phanerozoic Time.
1023   Patterns of Change in Earth Evolution 123–143. https://doi.org/10.1007/978-3-642-69317-
1024   5_8

1025   Holser, W.T., Magaritz, M., 1987. Events near the Permian-Triassic boundary. Marine
1026   Geology 11, 155–180.

1027   Holser, W. T., Schidlowski, M., Mackenzie, F. T., and Maynard, J. B., 1988, Geochemical
1028   cycles of carbon and sulfur, in Gregor, B. C., Garrels, R. M., Mackenzie, F. T., and Maynard,
1029   J. B., eds., Chemical Cycles in the Evolution of the Earth, John Wiley & Sons, p. 105-173.

1030   Horacek, M., Brandner, R., Abart, R., 2007. Carbon isotope record of the P/T boundary and
1031   the Lower Triassic in the Southern Alps: Evidence for rapid changes in storage of organic
1032   carbon. Palaeogeography, Palaeoclimatology, Palaeoecology 252, 347–354.
1033   https://doi.org/10.1016/j.palaeo.2006.11.049

1034   Horacek, M., Koike, T., Richoz, S., 2009. Lower Triassic $\delta^{13}C$ isotope curve from shallow-
1035   marine carbonates in Japan, Panthalassa realm: Confirmation of the Tethys $\delta^{13}C$ curve.
1036   Journal of Asian Earth Sciences 36, 481–490. https://doi.org/10.1016/j.jseaes.2008.05.005

1037   Horacek, M., Brandner, R., Richoz, S., Povoden-Karadeniz, E., 2010. Lower Triassic sulphur
1038   isotope curve of marine sulphates from the Dolomites, N-Italy. Palaeogeography,
1039   Palaeoclimatology, Palaeoecology 290, 65–70. https://doi.org/10.1016/j.palaeo.2010.02.016

1040 Horita, J., Zimmermann, H., Holland, H.D., 2002. Chemical evolution of seawater during the
1041 Phanerozoic. Geochimica et Cosmochimica Acta 66, 3733–3756.
1042 https://doi.org/10.1016/s0016-7037(01)00884-5

1043 Hurtgen, M.T., Pruss, S.B., Knoll, A.H., 2009. Evaluating the relationship between the carbon
1044 and sulfur cycles in the later Cambrian ocean: an example from the Port au Port Group,
1045 western Newfoundland, Canada. Earth Planet. Sci. Lett. 281, 288–97.

1046 Ingersoll, R.V., 2008. Subduction-related sedimentary basins of the USA Cordillera
1047 Sedimentary basins of the world. pp. 395-428. Netherlands: Elsevier: Amsterdam,
1048 Netherlands.

1049 Isozaki, Y., 1997. Permo-Triassic Boundary Superanoxia and Stratified Superocean: Records
1050 from Lost Deep Sea. Science 276, 235–238. https://doi.org/10.1126/science.276.5310.235

1051 Jattiot, R., Bucher, H., Brayard, A., Monnet, C., Jenks, J.F., Hautmann, M., 2016. Revision of
1052 the genus *Anasibirites Mojsisovics* (Ammonoidea): an iconic and cosmopolitan taxon of the
1053 late Smithian (Early Triassic) extinction. Papers in Palaeontology 2, 155–188.
1054 https://doi.org/10.1002/spp2.1036

1055 Jattiot, R., Bucher, H., Brayard, A., Brosse, M., Jenks, J.F., Bylund, K.G., 2017. Smithian
1056 ammonoid faunas from northeastern Nevada: implications for Early Triassic biostratigraphy
1057 and correlation within the western USA basin. Palaeontographica Abteilung A 309, 1–89.
1058 https://doi.org/10.1127/pala/309/2017/1

1059 Jenks, J.F., Monnet, C., Balini, M., Brayard, A., Meier, M., 2015. Biostratigraphy of Triassic
1060 Ammonoids. Topics in Geobiology 329–388. https://doi.org/10.1007/978-94-017-9633-0_13

1061 Jenks, J.F., Brayard, A., 2018. Smithian (Early Triassic) ammonoids from Crittenden Springs,
1062 Elko County, Nevada: Taxonomy, biostratigraphy and biogeography. New Mexico Museum
1063 of Natural History and Science, Bulletin, 78: 175pp.

1064 Johnston, D.T., 2005a. Multiple sulfur isotope fractionations in biological systems: A case
1065 study with sulfate reducers and sulfur disproportionators. American Journal of Science 305,
1066 645–660. https://doi.org/10.2475/ajs.305.6-8.645

1067 Johnston, D.T., Wing, B.A., Farquhar, J., Kaufman, A.J., Strauss, H., Lyons, T.W., Kah, L.C.,
1068 Canfield, D.E., 2005b. Active microbial sulfur disproportionation in the Mesoproterozoic.
1069 Science 310, 1477–79.

1070 Johnston, D.T., Poulton, S.W., Fralick, P.W., Wing, B.A., Canfield, D.E., Farquhar, J., 2006.
1071 Evolution of the oceanic sulfur cycle at the end of the Paleoproterozoic. Geochimica et
1072 Cosmochimica Acta 70, 5723–5739. https://doi.org/10.1016/j.gca.2006.08.001

1073 Johnston, D.T., Farquhar, J., Canfield, D.E., 2007. Sulfur isotope insights into microbial
1074 sulfate reduction: When microbes meet models. Geochimica et Cosmochimica Acta 71,
1075 3929–3947. https://doi.org/10.1016/j.gca.2007.05.008

Johnston, D.T., Farquhar, J., Habichr, K.S., Canfield, D.E., 2008a. Sulphur isotopes and the search for life: strategies for identifying sulphur metabolisms in the rock record and beyond. Geobiology 6, 425–435. https://doi.org/10.1111/j.1472-4669.2008.00171.x

Johnston, D.T., Farquhar, J., Summons, R.E., Shen, Y., Kaufman, A.J., Masterson, A.L., Canfield, D.E., 2008b. Sulfur isotope biogeochemistry of the Proterozoic McArthur Basin. Geochimica et Cosmochimica Acta 72, 4278–4290. https://doi.org/10.1016/j.gca.2008.06.004

Johnston, D.T., 2011. Multiple sulfur isotopes and the evolution of Earth's surface sulfur cycle. Earth-Science Reviews 106, 161–183. https://doi.org/10.1016/j.earscirev.2011.02.003

Jones, D.S., Fike, D.A., 2013. Dynamic sulfur and carbon cycling through the end-Ordovician extinction revealed by paired sulfate–pyrite δ^{34}S. Earth Planet. Sci. Lett. 363, 144–55.

Kampschulte, A., Strauss, H., 2004. The sulfur isotopic evolution of Phanerozoic seawater based on the analysis of structurally substituted sulfate in carbonates. Chemical Geology 204, 255–286. https://doi.org/10.1016/j.chemgeo.2003.11.013

Komatsu, T., Takashima, R., Shigeta, Y., Maekawa, T., Tran, H.D., Cong, T.D., Sakata, S., Dinh, H.D., Takahashi, O., 2016. Carbon isotopic excursions and detailed ammonoid and conodont biostratigraphies around Smithian–Spathian boundary in the Bac Thuy Formation, Vietnam. Palaeogeography, Palaeoclimatology, Palaeoecology 454, 65–74. https://doi.org/10.1016/j.palaeo.2016.04.017

Kummel, B., 1954. Triassic stratigraphy of southeastern Idaho and adjacent areas. US Government Printing Office.

Kummel, B., 1957. Chapter 16: Paleoecology of Lower Triassic Formations of Southeastern Idaho and Adjacent Areas. Geological Society of America Memoirs 437–468. https://doi.org/10.1130/mem67v2-p437

Kump, L.R., Pavlov, A., Arthur, M.A., 2005. Massive release of hydrogen sulfide to the surface ocean and atmosphere during intervals of oceanic anoxia. Geology 33, 397. https://doi.org/10.1130/g21295.1

Labidi, J., Cartigny, P., Birck, J.L., Assayag, N., Bourrand, J.J., 2012. Determination of multiple sulfur isotopes in glasses: A reappraisal of the MORB δ^{34}S. Chemical Geology 334, 189–198. https://doi.org/10.1016/j.chemgeo.2012.10.028

Leavitt, W.D., Halevy, I., Bradley, A.S., Johnston, D.T., 2013. Influence of sulfate reduction rates on the Phanerozoic sulfur isotope record. Proceedings of the National Academy of Sciences 110, 11244–11249. https://doi.org/10.1073/pnas.1218874110

Li, X., Gilhooly, W.P., Zerkle, A.L., Lyons, T.W., Farquhar, J., Werne, J.P., Varela, R., Scranton, M.I., 2010. Stable sulfur isotopes in the water column of the Cariaco Basin. Geochimica et Cosmochimica Acta 74, 6764–6778. https://doi.org/10.1016/j.gca.2010.08.020

Lin, X., PengG, J., Du, L., Yan, J., Hou, Z., 2017. Characterization of the Microbial Dolomite of the Upper Sinian Dengying Formation in the Hanyuan Area of Sichuan Province, China.

Acta Geologica Sinica - English Edition 91, 806–821. https://doi.org/10.1111/1755-6724.13311

Longinelli, A., Flora, O., 2007. Isotopic composition of gypsum samples of Permian and Triassic age from the north-eastern Italian Alps: Palaeoenvironmental implications. Chemical Geology 245, 275–284. https://doi.org/10.1016/j.chemgeo.2007.08.009

Lucas, S.G., Krainer, K., Milner, A.R., 2007. The type section and age of the Timpoweap Member and stratigraphic nomenclature of the Triassic Moenkopi Group in Southwestern Utah. New Mexico Museum of Natural History and Science Bulletin, 40, 109-117.

Luo, G., Kump, L.R., Wang, Y., Tong, J., Arthur, M.A., Yang, H., Huang, J., Yin, H., Xie, S., 2010. Isotopic evidence for an anomalously low oceanic sulfate concentration following end-Permian mass extinction. Earth and Planetary Science Letters 300, 101–111. https://doi.org/10.1016/j.epsl.2010.09.041

Lyons, T.W., Walter, L.M., Gellatly, A.M., Martini, A.M., Blake, R.E., 2004. Sites of anomalous organic remineralization in the carbonate sediments of South Florida, USA: The sulfur cycle and carbonate-associated sulfate. Special Paper 379: Sulfur Biogeochemistry - Past and Present 161–176. https://doi.org/10.1130/0-8137-2379-5.161

Machel, H.G., Krouse, H.R., Sassen, R., 1995. Products and distinguishing criteria of bacterial and thermochemical sulfate reduction. Applied Geochemistry 10, 373–389. https://doi.org/10.1016/0883-2927(95)00008-8

Marenco, P. J., 2007. Sulfur isotope geochemistry and the end Permian mass extinction. Ph. D. thesis, University of Southern California. p. 189.

Marenco, P.J., Corsetti, F.A., Kaufman, A.J., Bottjer, D.J., 2008. Environmental and diagenetic variations in carbonate associated sulfate: An investigation of CAS in the Lower Triassic of the western USA. Geochimica et Cosmochimica Acta 72, 1570–1582. https://doi.org/10.1016/j.gca.2007.10.033

McKee, E.D., 1954. Stratigraphy and history of the Moenkopi Formation of Triassic age. Geological Society of America Memoirs 1–126. https://doi.org/10.1130/mem61-p1

Meyer, K.M., Yu, M., Jost, A.B., Kelley, B.M., Payne, J.L., 2011. δ^{13}C evidence that high primary productivity delayed recovery from end-Permian mass extinction. Earth and Planetary Science Letters 302, 378–384. https://doi.org/10.1016/j.epsl.2010.12.033

Newton, R., Pevitt, E., Wignall, P., Bottrell, S., 2004. Large shifts in the isotopic composition of seawater sulphate across the Permo–Triassic boundary in northern Italy. Earth and Planetary Science Letters 218, 331–345. https://doi.org/10.1016/s0012-821x(03)00676-9

Ohmoto, H., 1992. Biogeochemistry of Sulfur and the Mechanisms of Sulfide-Sulfate Mineralization in Archean Oceans. Early Organic Evolution 378–397. https://doi.org/10.1007/978-3-642-76884-2_29

Ohmoto, H., Goldhaber, M.B., 1997. Sulfur and carbon isotopes. In: Barnes, H.L. (Ed.), Geochemistry of Hydrothermal Ore Deposits. Wiley, New York.

1151 Ono, S., Wing, B., Johnston, D., Farquhar, J., Rumble, D., 2006. Mass-dependent
1152 fractionation of quadruple stable sulfur isotope system as a new tracer of sulfur
1153 biogeochemical cycles. Geochimica et Cosmochimica Acta 70, 2238–2252.
1154 https://doi.org/10.1016/j.gca.2006.01.022

1155 Orchard, M.J., 2007. Conodont diversity and evolution through the latest Permian and Early
1156 Triassic upheavals. Palaeogeography, Palaeoclimatology, Palaeoecology 252, 93–117.
1157 https://doi.org/10.1016/j.palaeo.2006.11.037

1158 Ovtcharova, M., Bucher, H., Schaltegger, U., Galfetti, T., Brayard, A., Guex, J., 2006. New
1159 Early to Middle Triassic U–Pb ages from South China: Calibration with ammonoid
1160 biochronozones and implications for the timing of the Triassic biotic recovery. Earth and
1161 Planetary Science Letters 243, 463–475. https://doi.org/10.1016/j.epsl.2006.01.042

1162 Pakhomova, S.V., Hall, P.O.J., Kononets, M.U., Rozanov, A.G., Tengberg, A., Vershinin,
1163 A.V., 2007. Fluxes of iron and manganese across the sediment–water interface under various
1164 redox conditions, Marine Chemistry 107, 319-331.

1165 Pasquier, V., Sansjofre, P., Rabineau, M., Revillon, S., Houghton, J., Fike, D.A., 2017. Pyrite
1166 sulfur isotopes reveal glacial−interglacial environmental changes. Proceedings of the National
1167 Academy of Sciences 114, 5941–5945. https://doi.org/10.1073/pnas.1618245114

1168 Paull, R.A., Paull, R.K., 1993 Interpretation of Early Triassic nonmarine-marine relations,
1169 Utah, U.S.A. New Mexico Museum of Natural History and Science Bulletin, 3, 403–409.

1170 Payne, J., Kump, L., 2007. Evidence for recurrent Early Triassic massive volcanism from
1171 quantitative interpretation of carbon isotope fluctuations. Earth and Planetary Science Letters
1172 256, 264–277. https://doi.org/10.1016/j.epsl.2007.01.034

1173 Payne, J.L., 2004. Large Perturbations of the Carbon Cycle During Recovery from the End-
1174 Permian Extinction. Science 305, 506–509. https://doi.org/10.1126/science.1097023

1175 Petrash, D.A., Bialik, O.M., Bontognali, T.R.R., Vasconcelos, C., Roberts, J.A., McKenzie,
1176 J.A., Konhauser, K.O., 2017. Microbially catalyzed dolomite formation: From near-surface to
1177 burial. Earth-Science Reviews 171, 558–582. https://doi.org/10.1016/j.earscirev.2017.06.015

1178 Philippot, P., Van Zuilen, M., Lepot, K., Thomazo, C., Farquhar, J., Van Kranendonk, M.J.,
1179 2007. Early Archaean microorganisms preferred elemental sulfur, not sulfate. Science 317,
1180 1534–37.

1181 Poulton, S.W., Canfield, D.E., 2011. Ferruginous Conditions: A Dominant Feature of the
1182 Ocean through Earth's History. Elements 7, 107–112.
1183 https://doi.org/10.2113/gselements.7.2.107

1184 Present, T.M., Paris, G., Burke, A., Fischer, W.W., Adkins, J.F., 2015. Large Carbonate
1185 Associated Sulfate isotopic variability between brachiopods, micrite, and other sedimentary
1186 components in Late Ordovician strata. Earth and Planetary Science Letters 432, 187–198.
1187 https://doi.org/10.1016/j.epsl.2015.10.005

1188 Raiswell, R., Canfield, D., 2012. The iron biogeochemical cycle past and present. Geochem.
1189 Perspect. 1, 1–220.

1190 Retallack, G.J., Jahren, A.H., 2008. Methane Release from Igneous Intrusion of Coal during
1191 Late Permian Extinction Events. The Journal of Geology 116, 1–20.
1192 https://doi.org/10.1086/524120

1193 Riccardi, A.L., Arthur, M.A., Kump, L.R., 2006. Sulfur isotopic evidence for chemocline
1194 upward excursions during the end-Permian mass extinction. Geochimica et Cosmochimica
1195 Acta 70, 5740–5752. https://doi.org/10.1016/j.gca.2006.08.005

1196 Ries, J.B., Fike, D.A., Pratt, L.M., Lyons, T.W., Grotzinger, J.P., 2009. Superheavy pyrite
1197 ($^{34}S_{pyr} > {}^{34}S_{CAS}$) in the terminal Proterozoic Nama Group, southern Namibia: A consequence
1198 of low seawater sulfate at the dawn of animal life. Geology 37, 743–746.
1199 https://doi.org/10.1130/g25775a.1

1200 Rodriguez-Blanco, J.D., Shaw, S., Benning, L.G., 2015. A route for the direct crystallization
1201 of dolomite. American Mineralogist 100, 1172–1181. https://doi.org/10.2138/am-2015-4963

1202 Romano, C., Goudemand, N., Vennemann, T.W., Ware, D., Schneebeli-Hermann, E., Hochuli,
1203 P.A., Brühwiler, T., Brinkmann, W., Bucher, H., 2013. Climatic and biotic upheavals
1204 following the end-Permian mass extinction. Nature Geoscience 6, 57–60.
1205 https://doi.org/10.1038/ngeo1667

1206 Saitoh, M., Ueno, Y., Matsu'ura, F., Kawamura, T., Isozaki, Y., Yao, J., Ji, Z., Yoshida, N.,
1207 2017. Multiple sulfur isotope records at the end-Guadalupian (Permian) at Chaotian, China:
1208 Implications for a role of bioturbation in the Phanerozoic sulfur cycle. Journal of Asian Earth
1209 Sciences 135, 70–79. https://doi.org/10.1016/j.jseaes.2016.12.009

1210 Sansjofre, P., Cartigny, P., Trindade, R.I.F., Nogueira, A.C.R., Agrinier, P., Ader, M., 2016.
1211 Multiple sulfur isotope evidence for massive oceanic sulfate depletion in the aftermath of
1212 Snowball Earth. Nature Communications 7, 12192. http://dx.doi.org/10.1038/ncomms12192

1213 Schneebeli-Hermann, E., Hochuli, P.A., Bucher, H., Goudemand, N., Brühwiler, T., Galfetti,
1214 T., 2012. Palynology of the Lower Triassic succession of Tulong, South Tibet — Evidence
1215 for early recovery of gymnosperms. Palaeogeography, Palaeoclimatology, Palaeoecology
1216 339–341, 12–24. https://doi.org/10.1016/j.palaeo.2012.04.010

1217 Scholle, P.A., 1995. Carbon and Sulfur Isotope Stratigraphy of the Permian and Adjacent
1218 Intervals. The Permian of Northern Pangea 133–149. https://doi.org/10.1007/978-3-642-
1219 78593-1_9

1220 Schrag, D.P., Higgins, J.A., Macdonald, F.A., Johnston, D.T., 2013. Authigenic carbonate
1221 and the history of the global carbon cycle. Science 339, 540–543.

1222 Shen, Y., Buick, R., Canfield, D.E., 2001. Isotopic evidence for microbial sulphate reduction
1223 in the early Archaean era. Nature 410, 77–81.

1224 Shen, Y., Farquhar, J., Zhang, H., Masterson, A., Zhang, T., Wing, B.A., 2011. Multiple S-
1225 isotopic evidence for episodic shoaling of anoxic water during Late Permian mass extinction.
1226 Nature Communications 2, 210. https://doi.org/10.1038/ncomms1217

1227 Sim, M.S., Ono, S., Donovan, K., Templer, S.P., Bosak, T., 2011a. Effect of electron donors
1228 on the fractionation of sulfur isotopes by a marine Desulfovibrio sp. Geochimica et
1229 Cosmochimica Acta 75, 4244–4259. https://doi.org/10.1016/j.gca.2011.05.021

1230 Sim, M.S., Bosak, T., Ono, S., 2011b. Large Sulfur Isotope Fractionation Does Not Require
1231 Disproportionation. Science 333, 74–77. https://doi.org/10.1126/science.1205103

1232 Sim, M.S., Ono, S., Hurtgen, M.T., 2015. Sulfur isotope evidence for low and fluctuating
1233 sulfate levels in the Late Devonian ocean and the potential link with the mass extinction event.
1234 Earth and Planetary Science Letters 419, 52–62. https://doi.org/10.1016/j.epsl.2015.03.009

1235 Sobolev, S.V., Sobolev, A.V., Kuzmin, D.V., Krivolutskaya, N.A., Petrunin, A.G., Arndt,
1236 N.T., Radko, V.A., Vasiliev, Y.R., 2011. Linking mantle plumes, large igneous provinces and
1237 environmental catastrophes. Nature 477, 312–316. https://doi.org/10.1038/nature10385

1238 Song, H., Tong, J., Song, H., Qiu, H., Zhu, Y., 2010. Excursion of sulfur isotope
1239 compositions in the Lower Triassic of South Guizhou, China. Journal of Earth Science 21,
1240 158-160.

1241 Song, H., Wignall, P.B., Tong, J., Bond, D.P., Song, H., Lai, X., Zhang, K., Wang, H., Chen,
1242 Y., 2012. Geochemical evidence from bio-apatite for multiple oceanic anoxic events during
1243 Permian–Triassic transition and the link with end-Permian extinction and recovery. Earth and
1244 Planetary Science Letters 353, 12-21.

1245 Song, H., Tong, J., Algeo, T.J., Horacek, M., Qiu, H., Song, H., Tian, L., Chen, Z.-Q., 2013.
1246 Large vertical $\delta^{13}C_{DIC}$ gradients in Early Triassic seas of the South China craton: Implications
1247 for oceanographic changes related to Siberian Traps volcanism. Global and Planetary Change
1248 105, 7–20. https://doi.org/10.1016/j.gloplacha.2012.10.023

1249 Song, H., Wignall, P.B., Chu, D., Tong, J., Sun, Y., Song, H., He, W., Tian, L., 2014a.
1250 Anoxia/high temperature double whammy during the Permian-Triassic marine crisis and its
1251 aftermath. Scientific Reports 4. https://doi.org/10.1038/srep04132

1252 Song, H., Tong, J., Algeo, T.J., Song, H., Qiu, H., Zhu, Y., Tian, L, Lyons, T.W., Luo, G.,
1253 Kump, L. R., 2014b. Early Triassic seawater sulfate drawdown. Geochimica et
1254 Cosmochimica Acta 128, 95-113.

1255 Stanley, S.M., 2009. Evidence from ammonoids and conodonts for multiple Early Triassic
1256 mass extinctions. Proceedings of the National Academy of Sciences 106, 15264–15267.
1257 https://doi.org/10.1073/pnas.0907992106

1258 Strauss, H., 1997. The isotopic composition of sedimentary sulfur through time.
1259 Palaeogeography, Palaeoclimatology, Palaeoecology 132, 97–118.
1260 https://doi.org/10.1016/s0031-0182(97)00067-9

Sun, Y., Joachimski, M.M., Wignall, P.B., Yan, C., Chen, Y., Jiang, H., Wang, L., Lai, X., 2012. Lethally hot temperatures during the Early Triassic greenhouse. Science 338, 366–370. https://doi.org/10.1126/science.1224126

Sun, Y.D., Wignall, P.B., Joachimski, M.M., Bond, D.P.G., Grasby, S.E., Sun, S., Yan, C.B., Wang, L.N., Chen, Y.L., Lai, X.L., 2015. High amplitude redox changes in the late Early Triassic of South China and the Smithian–Spathian extinction. Palaeogeography, Palaeoclimatology, Palaeoecology 427, 62–78. https://doi.org/10.1016/j.palaeo.2015.03.038

Takahashi, S., Kaiho, K., Hori, R.S., Gorjan, P., Watanabe, T., Yamakita, S., Aita, Y., Takemura, A., Spörli, K.B., Kakegawa, T., Oba, M., 2013. Sulfur isotope profiles in the pelagic Panthalassic deep sea during the Permian–Triassic transition. Global and Planetary Change 105, 68–78. https://doi.org/10.1016/j.gloplacha.2012.12.006

Thomazo, C., Vennin, E., Brayard, A., Bour, I., Mathieu, O., Elmeknassi, S., Olivier, N., Escarguel, G., Bylund, K.G., Jenks, J., Stephen, D.A., Fara, E., 2016. A diagenetic control on the Early Triassic Smithian-Spathian carbon isotopic excursions recorded in the marine settings of the Thaynes Group (Utah, USA). Geobiology 14, 220–236. https://doi.org/10.1111/gbi.12174

Tian, L., Tong, J., Algeo, T.J., Song, H., Song, H., Chu, D., Shi, L., Bottjer, D.J., 2014. Reconstruction of Early Triassic ocean redox conditions based on framboidal pyrite from the Nanpanjiang Basin, South China. Palaeogeography, Palaeoclimatology, Palaeoecology 412, 68–79. https://doi.org/10.1016/j.palaeo.2014.07.018

Tong, J., Zuo, J., Chen, Z., 2007. Early Triassic carbon isotope excursions from South China: proxies for devastation and restoration of marine ecosystems following the end-Permian mass extinction. Geological Journal 42, 371-389.

Tostevin, R., Turchyn, A. V., Farquhar, J., Johnston, D. T., Eldridge, D. L., Bishop, J. K., McIlvin, M., 2014. Multiple sulfur isotope constraints on the modern sulfur cycle. Earth and planetary science letters 396, 14-21.

Tozer, E.T., 1982. Marine Triassic faunas of North America: Their significance for assessing plate and terrane movements. Geologische Rundschau 71, 1077–1104. https://doi.org/10.1007/bf01821119

Tribovillard, N., Algeo, T.J., Lyons, T., Riboulleau, A., 2006. Trace metals as paleoredox and paleoproductivity proxies: An update. Chemical Geology 232, 12–32. https://doi.org/10.1016/j.chemgeo.2006.02.012

Vasconcelos, C., McKenzie, J.A., 1997. Microbial mediation of modern dolomite precipitation and diagenesis under anoxic conditions (Lagoa Vermelha, Rio de Janeiro, Brazil) J. Sediment. Res. 67, 378-390.

van de Velde, S., Meysman, F.J.R., 2016. The Influence of Bioturbation on Iron and Sulphur Cycling in Marine Sediments: A Model Analysis. Aquatic Geochemistry 22, 469–504. https://doi.org/10.1007/s10498-016-9301-7

Vennin, E., Olivier, N., Brayard, A., Bour, I., Thomazo, C., Escarguel, G., Fara, E., Bylund, K.G., Jenks, J.F., Stephen, D.A., Hofmann, R., 2015. Microbial deposits in the aftermath of the end-Permian mass extinction: A diverging case from the Mineral Mountains (Utah, USA). Sedimentology 62, 753–792. https://doi.org/10.1111/sed.12166

Wignall, P.B., Bond, D.P.G., Sun, Y., Grasby, S.E., Beauchamp, B., Joachimiski, M.M., Blomeier, D.P.G., 2016. Ultra-shallow-marine anoxia in an Early Triassic shallow-marine clastic ramp (Spitsbergen) and the suppression of benthic radiation. Geological Magazine 153, 316–331. https://doi.org/10.1017/s0016756815000588

Wilgus, C. K., 1981. A stable isotope study of Permian and Triassic marine evaporite and carbonate rocks, Western Interior, U.S.A., PhD thesis: University of Oregon, Eugene, OR, 109 p.

Winguth, C., Winguth, A.M.E., 2012. Simulating Permian–Triassic oceanic anoxia distribution: Implications for species extinction and recovery. Geology 40, 127–130. https://doi.org/10.1130/g32453.1

Wu, N., Farquhar, J., Strauss, H., Kim, S.-T., Canfield, D.E., 2010. Evaluating the S-isotope fractionation associated with Phanerozoic pyrite burial. Geochimica et Cosmochimica Acta 74, 2053–2071. https://doi.org/10.1016/j.gca.2009.12.012

Zerkle, A.L., Farquhar, J., Johnston, D.T., Cox, R.P., Canfield, D.E., 2009. Fractionation of multiple sulfur isotopes during phototrophic oxidation of sulfide and elemental sulfur by a green sulfur bacterium. Geochimica et Cosmochimica Acta 73, 291–306. https://doi.org/10.1016/j.gca.2008.10.027

Zerkle, A.L., Kamyshny, A., Kump, L.R., Farquhar, J., Oduro, H., Arthur, M.A., 2010. Sulfur cycling in a stratified euxinic lake with moderately high sulfate: Constraints from quadruple S isotopes. Geochimica et Cosmochimica Acta 74, 4953–4970. https://doi.org/10.1016/j.gca.2010.06.015

Zerkle, A.L., Jones, D.S., Farquhar, J., Macalady, J.L., 2016. Sulfur isotope values in the sulfidic Frasassi cave system, central Italy: A case study of a chemolithotrophic S-based ecosystem. Geochimica et Cosmochimica Acta 173, 373–386. https://doi.org/10.1016/j.gca.2015.10.028

Zhang, F., Xu, H., Konishi, H., Kemp, J.M., Roden, E.E., Shen, Z., 2012. Dissolved sulfide-catalyzed precipitation of disordered dolomite: Implications for the formation mechanism of sedimentary dolomite. Geochimica et Cosmochimica Acta 97, 148–165. https://doi.org/10.1016/j.gca.2012.09.008

Zhang, G., Zhang, X., Hu, D., Li, D., Algeo, T.J., Farquhar, J., Henderson, C.M., Qin, L., Shen, M., Shen, D., Schoepfer, S.D., Chen, K., Shen, Y., 2017. Redox chemistry changes in the Panthalassic Ocean linked to the end-Permian mass extinction and delayed Early Triassic biotic recovery. Proceedings of the National Academy of Sciences 114, 1806–1810. https://doi.org/10.1073/pnas.1610931114

1337 Zhang, G., Zhang, X., Li, D., Farquhar, J., Shen, S., Chen, X., Shen, Y., 2015. Widespread
1338 shoaling of sulfidic waters linked to the end-Guadalupian (Permian) mass extinction. Geology
1339 G37284.1. https://doi.org/10.1130/g37284.1

1340 Zhao, M.-Y., Zheng, Y.-F., Zhao, Y.-Y., 2016. Seeking a geochemical identifier for
1341 authigenic carbonate. Nature Communications 7, 10885.
1342 https://doi.org/10.1038/ncomms10885

1343 Zhou, C., Jiang, S., Xiao, S., Chen, Z., Yuan, X., 2012. Rare earth elements and carbon
1344 isotope geochemistry of the Doushantuo Formation in South China: Implication for middle
1345 Ediacaran shallow marine redox conditions. Chinese Science Bulletin 57, 1998–2006.
1346 https://doi.org/10.1007/s11434-012-5082-6

1347 Zonneveld, J.-P., Gingras, M.K., Beatty, T.W., 2010. Diverse ichnofossil assemblages
1348 following the P-T mass extinction, lower Triassic, Alberta and British Columbia, Canada:
1349 Evidence for shallow marine refugia on the Northwestern coast of Pangaea. Palaios 25, 368–
1350 392. https://doi.org/10.2110/palo.2009.p09-135r

1351

1352 **Captions**

1353 **Table 1.** Results of isotopic and elemental analyses.

1354

1355 **Fig. 1:** Chronostratigraphic subdivisions of the Early Triassic (radiometric ages by

1356 Ovtcharova et al., 2006, Galfetti et al., 2007a and Burgess et al., 2014) with previously

1357 published carbon isotope trends after Galfetti et al., 2007; Grasby et al., 2013 and Caravaca et

1358 al., 2017a showing that similar fluctuations are observed worldwide from various localities

1359 (see palaeogeographic map modified after Brayard et al., 2006). Subdivisions of the Smithian

1360 and Spathian follow the ammonoid zonation from Brühwiler et al. (2010) and Guex et al.

1361 (2010). l.: lower; mi.: middle; u.: upper. The definition of the Dienerian/Smithian Boundary

1362 (DSB) follows biostratigraphical data published in e.g., Galfetti et al. (2007) and Romano et

1363 al. (2013). A formal definition of the DSB is under discussion and some authors have

1364 proposed to place this boundary at, or just below, the "P2" δ^{13}C isotopic maximum (e.g., Song

1365 et al., 2013). The middle-late Smithian and Smithian-Spathian Boundary (SSB) correlation

1366 among localities is primarily based on high-resolution ammonoid zonations (see synthesis in

1367 Jenks et al., 2015).

1368

1369 **Fig. 2:** **(A)** Early Triassic paleogeographic map and location of the Sonoma Foreland Basin

1370 (SFB), modified after Brayard et al. (2013). **(B)** Simplified paleogeographic map of the SFB

1371 with location of the Mineral Mountains section (after Caravaca et al., 2017b).

1372

1373 **Fig. 3:** Mineral Mountains section with corresponding lithological units and

1374 chemostratigraphic parameters. See Vennin et al. (2015) for detailed information on facies

1375 and depositional environments. Abbreviations for the sequential framework: SB: sequence

1376 boundary; MFS: maximum flooding surface. Abbreviations for the ammonoid zones: *V.u.*:

1377 *Vercherites undulatus* bed; *I.b.*: *Inyoites beaverensis* beds; *O.*: *Owenites* beds; *A.m.*:

1378 *Anasibirites multiformis* beds; Xe: Xenoceltitidae "*gen. indet.*" A. beds (see Brayard et al.,

1379 2013 and Jattiot et al., 2016). Relative variations of sea surface temperatures are depicted

1380 using color gradient and underlined a major cooling event across the Smithian/Spathian

1381 Boundary (interpreted from Sun et al., 2012 and Romano et al., 2013). A prolonged absence

1382 of bioturbation occurred in the SSB and lower unit C intervals. These deposits correspond to

1383 mud outer ramp lower offshore environment (Vennin et al., 2015). Below and above, the

1384 depositional environment is the same but shows a more intense bioturbation.

1385

1386 **Fig. 4:** Cross calibration between SO_2-EA-IRMS and SF_6-IRMS on the $\delta^{34}S$ values of 10

1387 samples from this study. Uncertainties are smaller than the symbol size.

1388

1389 **Fig. 5:** Relationship between the $\delta^{13}C_{carb}$ (VPDB, ‰) and the Mg/(Mg+Ca) ratio in units A, B,

1390 SSB and C.

1391

Fig. 6: Correlation relationship between the carbonate content (in wt. %) and the sum of calcium and magnesium content (in wt. %).

1394

Fig. 7: Selected thin sections from the Mineral Mountains section under a photonic and scanning electron microscope. **(A-B-C)** Burrows underlying a strong remobilization of the sediments during bioturbation (white-dash line) and pervasive microdolomitization (black arrows) in sample from a micropackstone of the unit B mudstone. **(D)** Non-biotic and non-bioturbated mudstone from the SSB unit. **(C, F-E)** SEM backscattered electron images of pyrite framboids from units B and SSB.

1401

Fig. 8: Graphic showing the sulfides $\delta^{34}S$ and $\Delta^{33}S$ relationship in units A, B, SSB and C. The grey stars and the pale blue square respectively represent the average Early Triassic sedimentary sulfides and seawater sulfate multiple sulfur isotope signatures estimated by model calculations (Wu et al., 2010). The red dashed curve represents the mixing line of these two endmembers. The black solid curve displays isotopic values of accumulative sulfides produced during a Rayleigh-type distillation of the residual sulfate pool (assuming values estimated by the model calculations) in a closed system, with MSR $^{34}\varepsilon$ and $^{33}\lambda$ values of 44.8‰ and 0.512 (red arrow), respectively. Numbers on this black solid curve correspond to the fraction of sulfates converted to sulfides. The dashed black curves depict mixing lines of accumulative sulfides produced in closed system and sulfides produced in an open system with respect to sulfates. The black and blue arrows respectively represent the evolution of instantaneously produced hydrogen sulfides and the residual sulfates during a Rayleigh-type distillation in closed system.

1415

1416   **Fig. 9:** Relationships between the $\delta^{34}S_{CAS}$ (VCDT, ‰) and the Mg/(Mg+Ca) ratio **(A),** and

1417   the Mn/Sr ratio **(B)** in units A, B, SSB and C.

1418
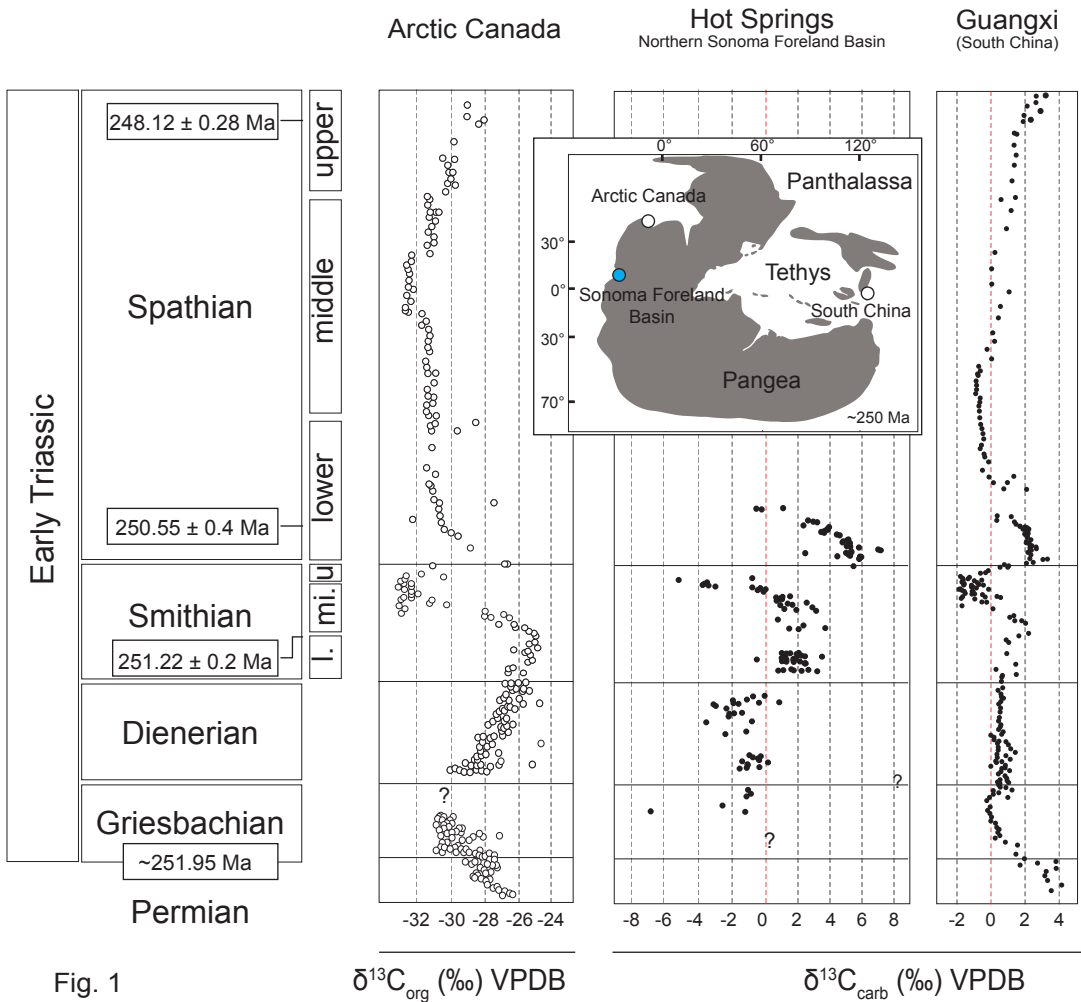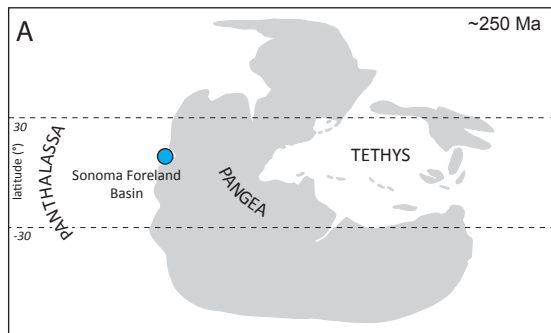
Fig. 1

Arctic Canada

Hot Springs
Northern Sonoma Foreland Basin

Guangxi
(South China)

Early Triassic

248.12 ± 0.28 Ma

upper

Spathian

middle

lower

250.55 ± 0.4 Ma

Smithian

u. | mi. | l.

251.22 ± 0.2 Ma

Dienerian

Griesbachian

~251.95 Ma

Permian

δ¹³C$_{org}$ (‰) VPDB

δ¹³C$_{carb}$ (‰) VPDB

Panthalassa

Arctic Canada

0°   60°   120°

30°

0°

Tethys

Sonoma Foreland Basin

South China

30°

Pangea

70°

~250 Ma
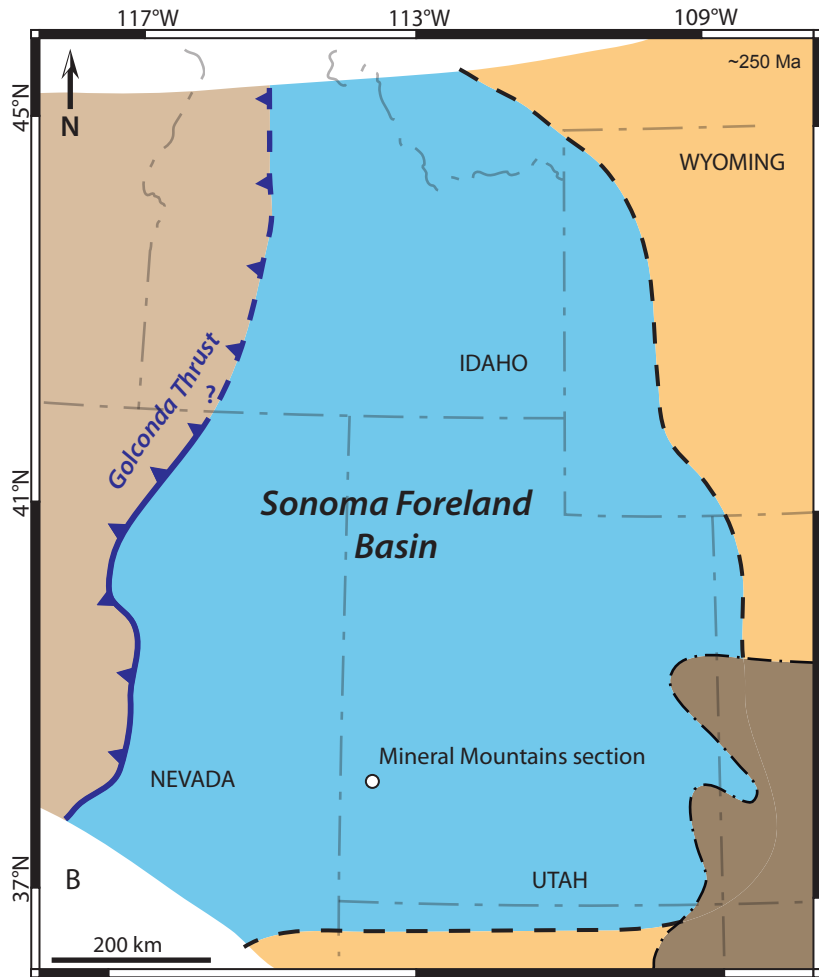
Fig. 2

Fig. 3

Fig. 4

Fig. 5

Fig. 6

Fig. 7

A

500 μm

B

75 μm

C

5 μm

Unit B
MI111
83 m depth

Unit SSB

MI151
116 m depth

F

MI127 / 107.7 m depth

20 μm

D

500 μm

E

10 μm
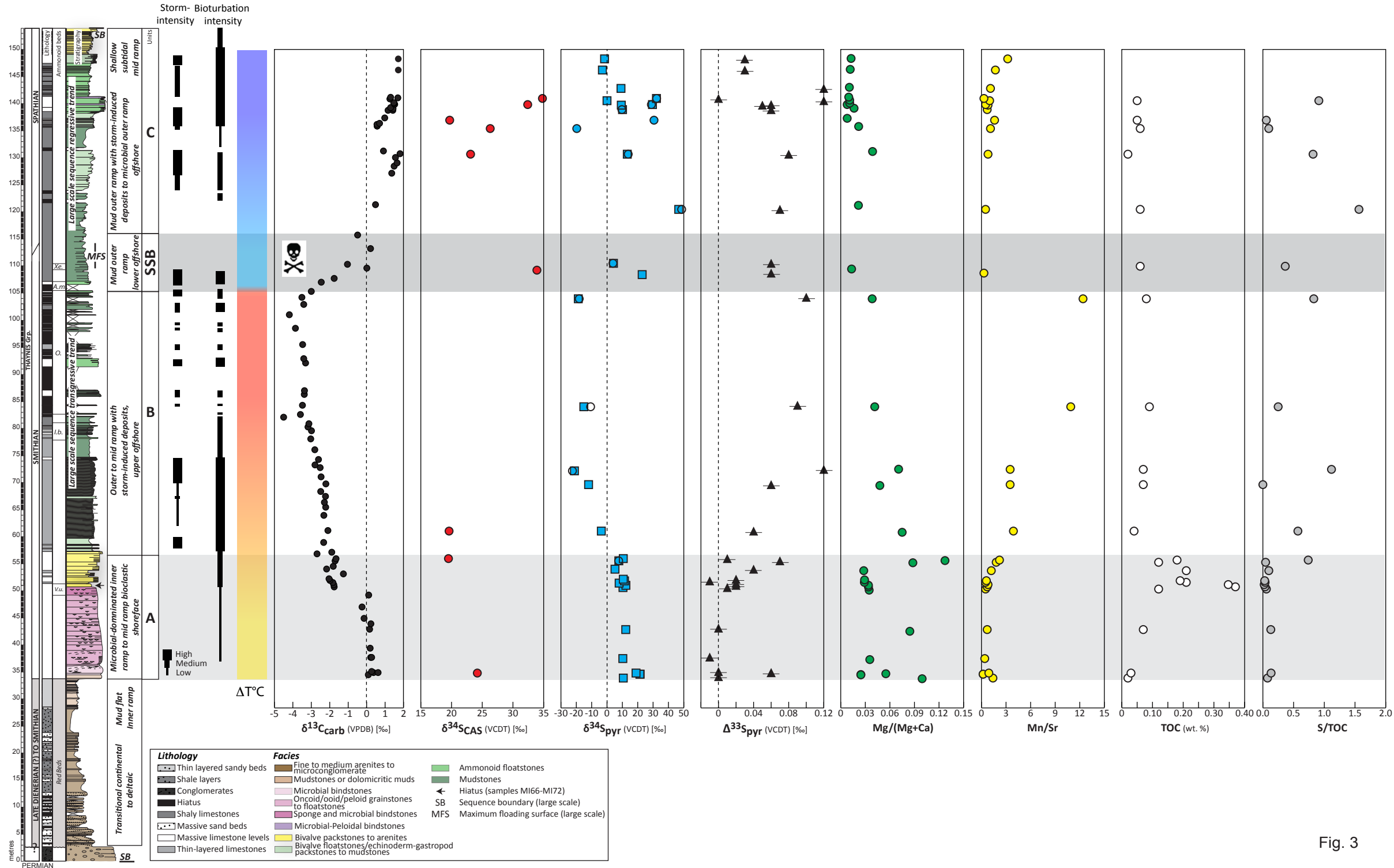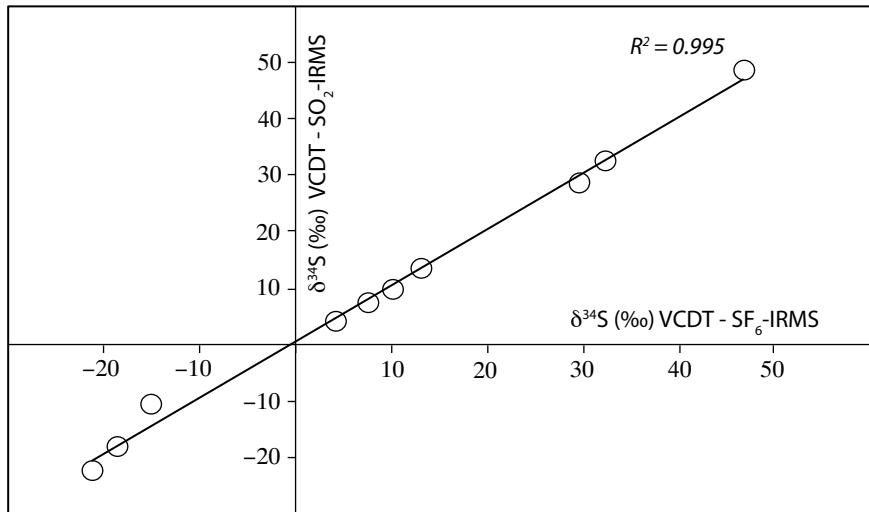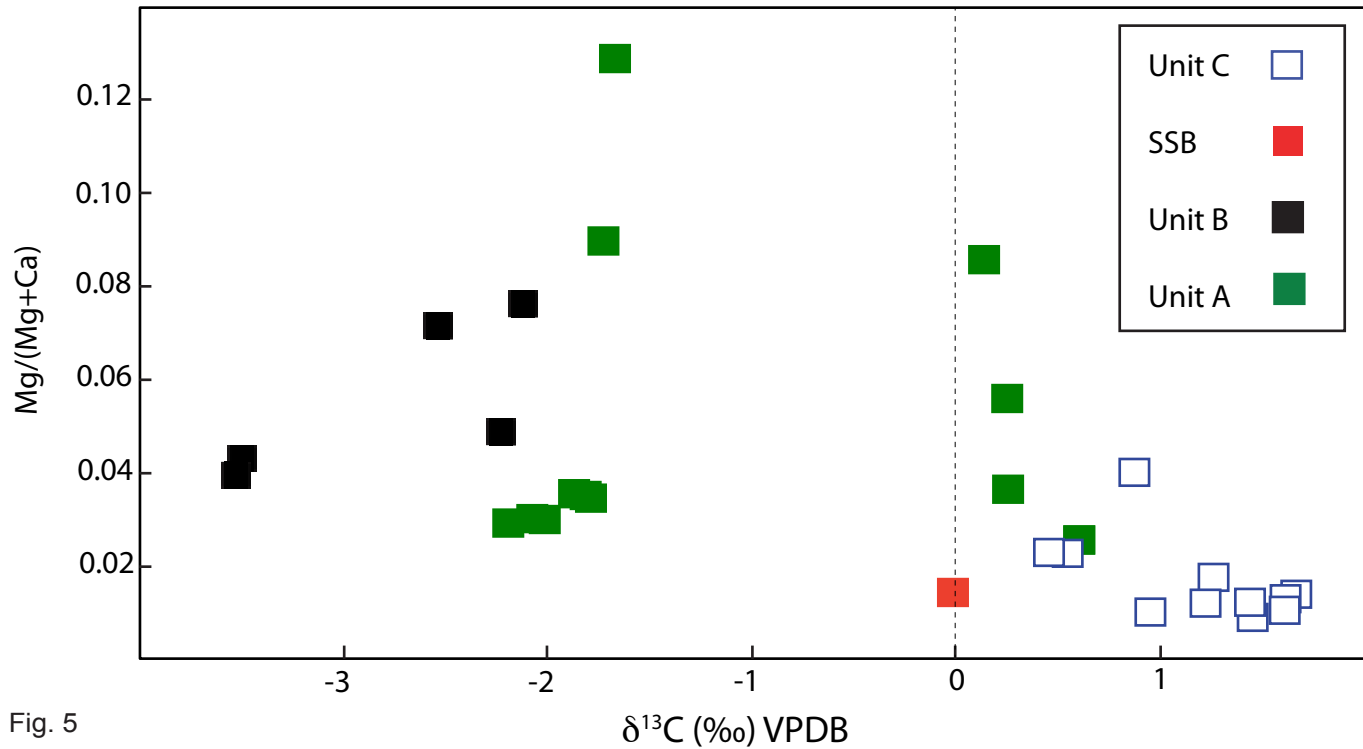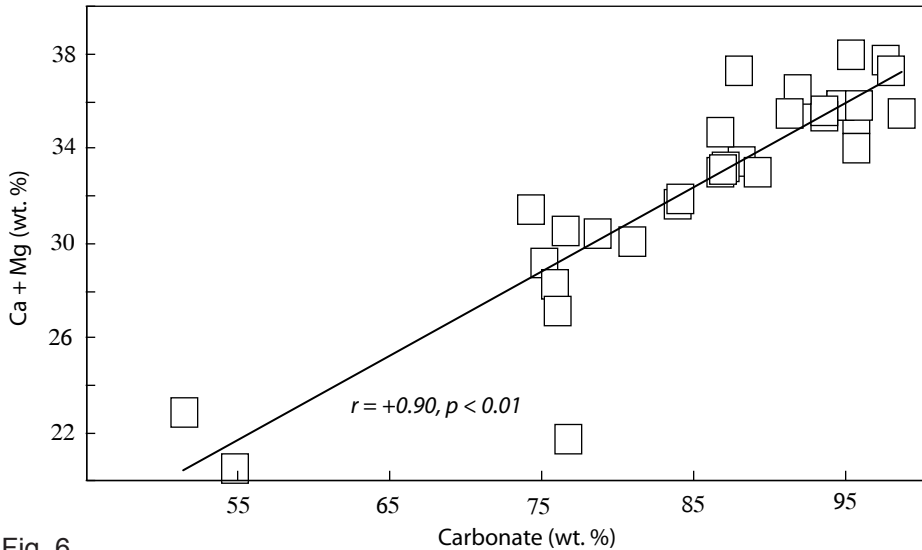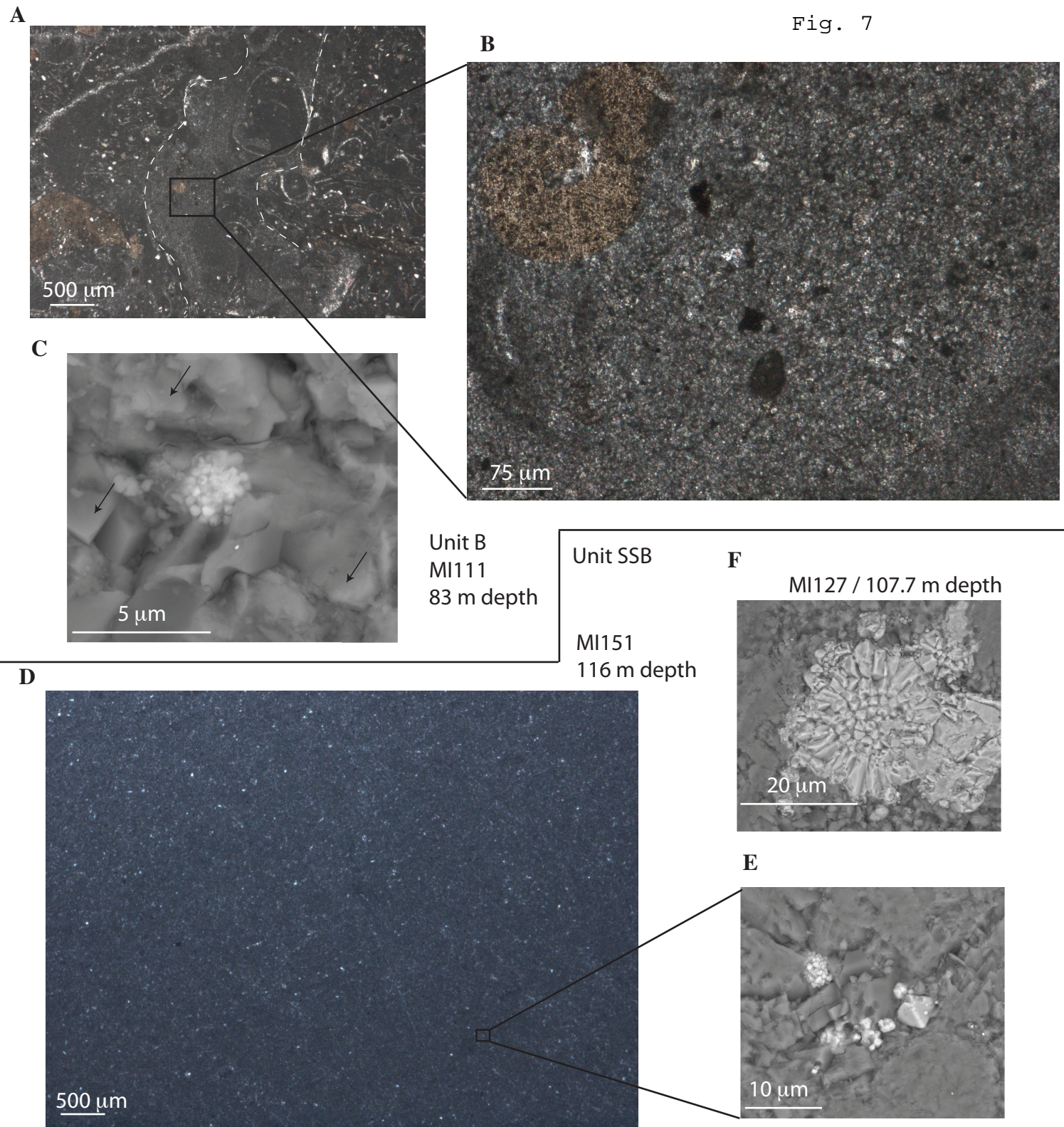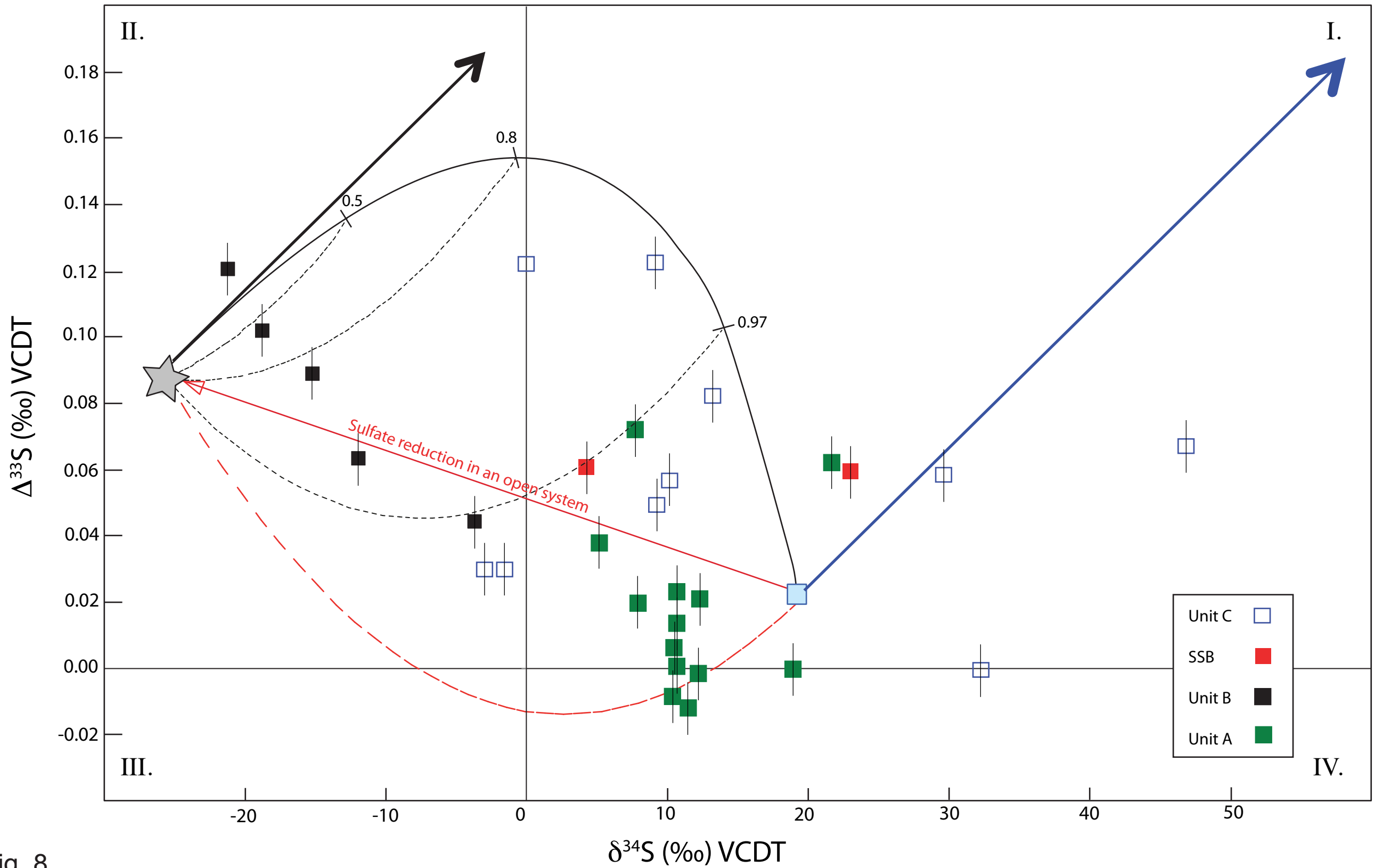
Fig. 8
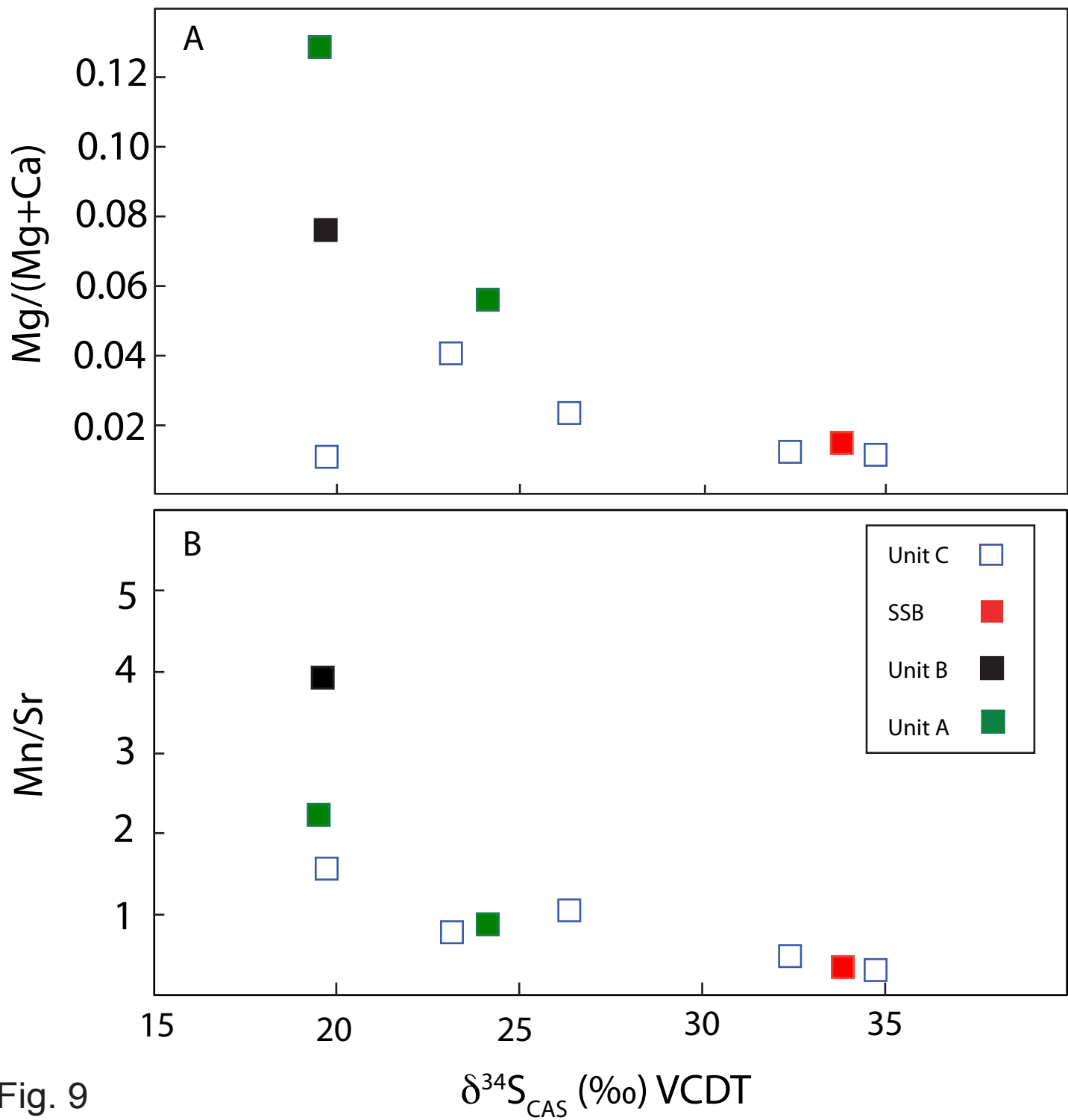
Fig. 9

Table 1 : Participant's baseline characteristics

	EIH (n = 10)	NEIH (n = 9)	Untrained (n = 10)
Age (years)	40.3 ± 1.2	39.1 ± 1.3	37.8 ± 1.7
Body mass (kg)	70.1 ± 2.3	71.1 ± 2.4	76.3 ± 1.9
Height (cm)	178 ± 2	179 ± 2	174 ± 1
Body mass index ($kg \cdot m^{-2}$)	22.2 ± 0.4 [Ψ]	22.3 ± 0.7 [Ψ]	24.9 ± 0.6
VO_2max ($ml \cdot min^{-1} \cdot kg^{-1}$)	60.1 ± 2.0 [Ψ]	58.3 ± 1.8 [Ψ]	43.3 ± 2.0
FEV_1 (% predicted)	119 ± 3	112 ± 7	114 ± 6
Training volume ($hours \cdot week^{-1}$)	12.0 ± 1.7 [Ψ]	11.3 ± 1.1 [Ψ]	2 ± 0.5

Values are means ± SEM. EIH: athletes exhibiting O_2 desaturation; NEIH: athletes without O_2 desaturation

[Ψ], significantly different from untrained group ($p < 0.05$)